Ore Geology Reviews 112 (2019) 103028

Contents lists available at ScienceDirect

Ore Geology Reviews

journal homepage: www.elsevier.com/locate/oregeorev

Controls on and prospectivity mapping of volcanic-type uranium mineralization in the Pucheng district, NW Fujian, China

Jiangnan Zhao[a,*], Shouyu Chen[a,b], Renguang Zuo[b], Mi Zhou[c]

[a] School of Earth Resources, China University of Geosciences, Wuhan 430074, China
[b] State Key Laboratory of Geological Processes and Mineral Resources, China University of Geosciences, Wuhan 430074, China
[c] 294th Geological Party of Fujian Nuclear Industry, Nanping 353000, China

ARTICLE INFO

Keywords:
L-function
Fry analysis
Fractal analysis
Artificial neural network
Uranium prospectivity mapping
NW Fujian

ABSTRACT

A number of volcanic-type uranium deposits occur in Pucheng district, Fujian province, China. Structural controls and volcanic rocks clearly explain the uranium mineralization in this area. To explore the subtle spatial associations of uranium occurrences with certain geological features, these uranium deposits were subjected to *L*–function, Fry, and fractal analyses. The results reveal that (1) these deposits are clustered, have a bifractal distribution, and are spatially parallel to the NE-striking faults, (2) the regional-scale NE-striking, and prospect-scale NE-, and NW-striking faults exhibit significant spatial associations with uranium deposits as illustrated by the Fry models; (3) intersections of the faults with larger permeability and connectivity promote the mineralization process, and (4) the spatial complexities of structures and lithological contacts, quantified by the fractal dimension, form strong and positive correlations with uranium occurrences and sizes. Finally, by integrating nine spatial evidential layers representing the controlling factors for the occurrence of mineralization, the artificial neural network model was applied to map mineral prospectivity for the uranium mineralization. The receiver operating characteristics (ROC) curve and the under the ROC curve (AUC) were utilized to measure the performance of the prospectivity models. The model is highly capable of mapping uranium prospectivity because the AUC is greater than 0.5 and close to 1. The prospectivity mapping confirmed that there is significant potential for uranium mineralization in the study area, which opens up new avenues for further explorations on uranium deposits in Pucheng district.

1. Introduction

Mineral prospectivity mapping (MPM) is a multi-step process that involves generating, weighting, and integrating mappable features to delineate target areas at a given scale (Bonham-Carter, 1994; Carranza et al., 2009; Carranza, 2011; Zuo and Carranza, 2011; Ford et al., 2016). However, ascertaining appropriate prospecting criteria that can appropriately represent the mineral deposit-type sought to generate a set of evidential layers is a fundamental issue encountered during MPM (Bonham-Carter, 1994; Carranza et al., 2008; Carranza and Sadeghi, 2010; Yousefi and Nykänen, 2017). To address this issue, a mineral systems approach was proposed for the identification of crucial targeting criteria, and its major components are as follows (Wyborn et al., 1994; McCuaig et al. 2010; Porwal et al., 2015): (i) sources of mineralizing fluids and transporting ligands; (ii) sources of metals and other ore components; (iii) energy gradients that drive the movement of fluids; (iv) migration pathways including inflow and outflow zones for large amount of fluids; (v) physical and chemical traps for ore precipitation; and finally (vi) preservation of the deposits. Modeling the spatial distribution of known mineral deposits associated with geological features can also provide insights into the exploration criteria (Carlson, 1991; Vearncombe and Vearncombe, 1999; Carranza et al., 2008; Parsa et al., 2018). Till date, fractal (Mandelbrot, 1983), point pattern (Diggle, 1983), and Fry (1979) analyses have been carried out for evaluating the spatial distribution of mineral deposits (Vearncombe & Vearncombe, 1999; Kreuzer et al., 2007; Carranza et al., 2009; Zuo et al., 2009b; Wang et al., 2015). Another fundamental issue includes difficulty in integration of various evidential layers to model the prospectivity or likelihood of mineral occurrences (Bonham-Carter et al., 1989; Zuo et al., 2009a; Zuo and Carranza, 2011; Carranza and Laborte, 2015). Two main approaches, namely data- and knowledge-driven approaches, are available to address this issue associated with MPM (e.g., Bonham-Carter, 1994; Porwal et al., 2003a; Carranza, 2004; Carranza and Sadeghi, 2010; Porwal and Kreuzer, 2010; Wang et al., 2017). The

* Corresponding author.
E-mail address: zhaojn@cug.edu.cn (J. Zhao).

https://doi.org/10.1016/j.oregeorev.2019.103028
Received 28 August 2018; Received in revised form 27 April 2019; Accepted 19 July 2019
Available online 06 August 2019

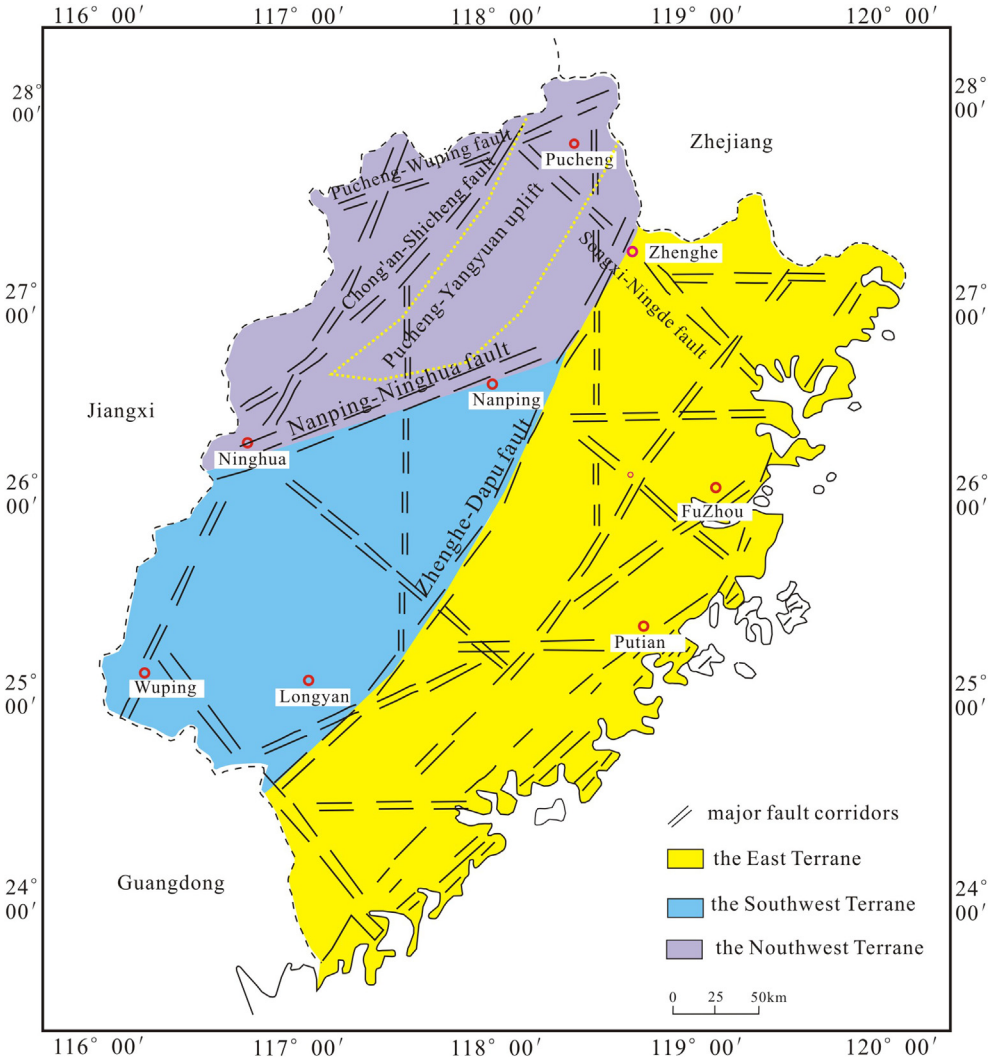

Fig. 1. The geographic location and the simplified geological map of Fujian Province, China (after BGMRFJ, 1985; Wei et al., 1997).

data-driven methods, involve the use of known mineral deposits in a region of interest, as training sites to establish spatial relationships between the known deposits and evidential layers (Agterberg et al., 1990; Cheng and Agterberg, 1999; Brown et al., 2000; Carranza et al., 2005; Oh and Lee, 2010; Harris et al., 2015; Zhang et al., 2016). In contrast, the knowledge-driven methods are based on the expert judgments in discretization of continuous spatial values into arbitrary classes and then assigning the same weight to all values in each class of evidential layers (Lisitsin et al., 2014; Asadi et al., 2016; Du et al., 2016; Yousefi and Carranza, 2017).

Volcanic-type uranium deposits, accounting for ~17.6% of identified uranium resources in China, are one of the four major types of uranium deposits in China, and the others include granite (~22.9%), sandstone (~43%), and carbonaceous–siliceous–pelitic (~8.7%) types (Cai et al., 2015; Fu et al., 2015). The Pucheng district in Fujian Province, characterized by widespread volcanics, is a significant area rich in volcanic-type uranium resources in the South China uranium province. Uranium mineralization was discovered in the late 1950s and has been mined for decades in this area (Xiao and Wang, 1998; Zhou, 2012). Extensive research efforts have been devoted to identify the source of uranium within such deposits (Leroy and George-Aniel, 1992; Lu et al., 1997; Nash, 2010; Maithani and Srinivasan, 2011). Numerous mineral explorations and scientific studies have shown that these type deposits often occur at lithological interfaces and in volcanic structures within rhyodacite, lava, and subvolcanic rocks in collapsed volcanic basins (Finch et al., 1993; Huang, 2010; Nash, 2010; Li et al., 2012; Zhou, 2012).

In this study, *L*–function, Fry, and fractal analyses were carried out to explore the spatial patterns of known uranium occurrences in Pucheng district, NW Fujian, China. The data-driven artificial neural network (ANN) model was then applied for the potential mapping of uranium. The main objectives of this study include the demonstration of the geological controls on occurrence of volcanic-type uranium on one hand, and generation of uranium prospectivity targets for further exploration on the other.

2. Geological background

2.1. Regional geological setting

The study region located in Pucheng district (27°25′–28°20′N and 117°50′–118°50′E), approximately covers an area of 7000 km^2, and is situated in the northwestern region of Fujian Province, China. Geologically, the area belongs to the northeastern part of the Cathaysia Block, and is adjacent to Jiangshan–Shaoxing fault zone and the Yangtze Block to the north (Liu et al., 2010). The Zhenghe–Dapu and the Nanping–Ninghua faults define the boundaries of the three terranes (NW-, SW-, and E-) in Fujian province based on different lithologies, formations, deformation characteristics, and tectonic evolutions (BGMRFJ, 1985; Zhang et al., 2008) (Fig. 1). The dominant strata and

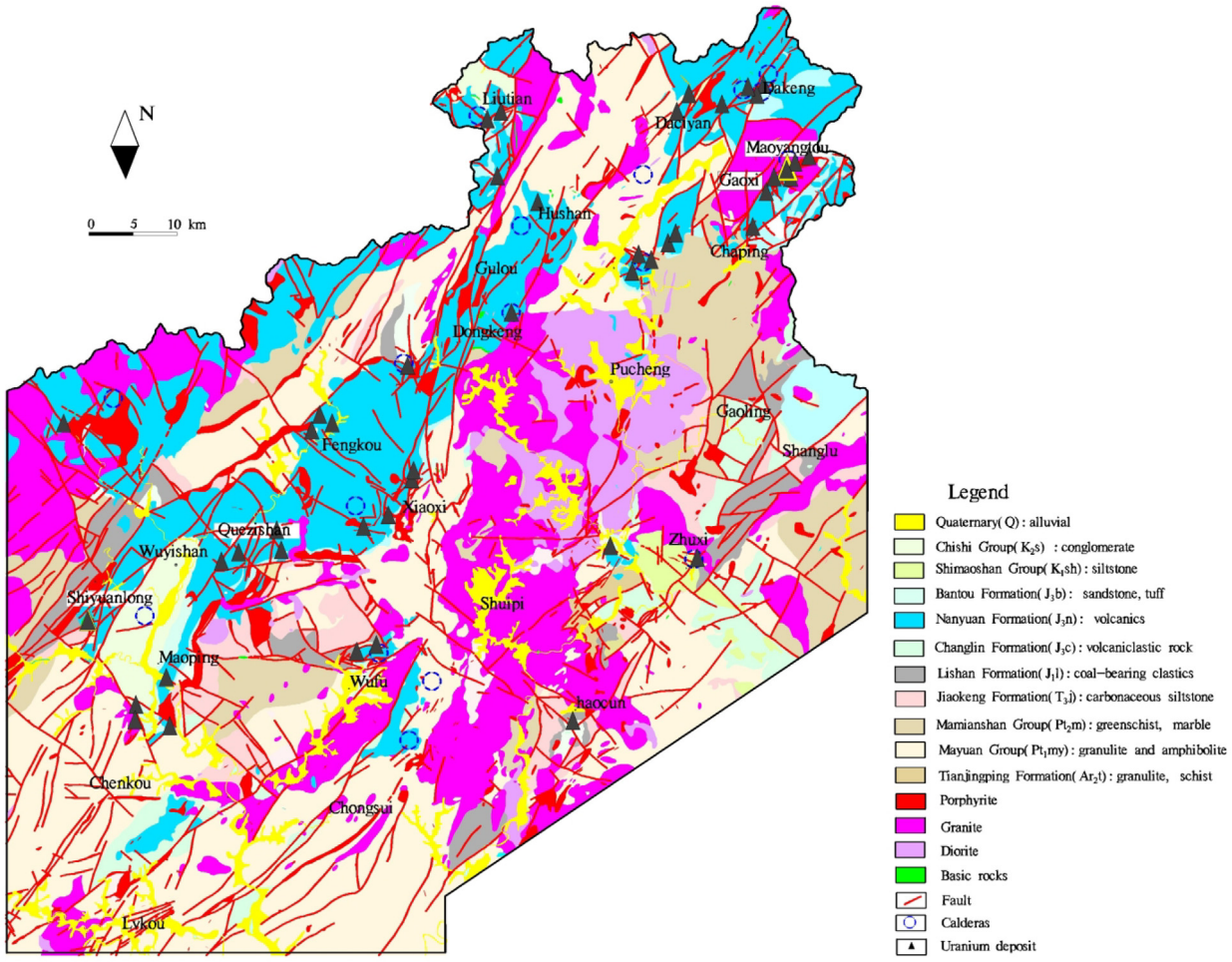

Fig. 2. Simplified geological map of Pucheng district (modified from the study of Zhou, 2012).

outcrops in the NW-terrain include the Archean–Proterozoic metamorphic basements and Mesozoic sedimentary covers; however, the Late Paleozoic to Early Mesozoic strata are missing due to the effect of long-term uplift and denudation that occurred during this period (Wei et al., 1997; Zhang et al., 2008). This district has experienced three stages of tectonic–magmatic evolution, including the basement forming stage from the Late Achaean to the Early Paleozoic, the platform cover forming stage from the Late Palaeozoic to the Early Mesozoic, and finally the active continental margin stage since the Late Mesozoic (BGMRFJ, 1985; Wei et al., 1997).

2.2. Lithostratigraphy

The strata of this area are dominated by the Archean–Proterozoic metamorphic basement, unconformably overlain by the Mesozoic volcanic rocks. The metamorphic basement consists of Tianjingping Formation (Ar_2t), Mayuan Group (Pt_1my), and Mamianshan Group (Pt_2mm). They are characterized by low to high grade metamorphic rocks including sericite schist, metamorphic sandstone, metamorphosed siltstone, metamorphic conglomerate, phyllite, amphibolites, and granulite. The Tianjingping Formation is composed mainly of the biotite plagioclase granulite. The Mayuan Group consists of the Dajinshan Formation (Pt_1d) and the Nanshan Formation (Pt_1n) with a conformity. The former is characterized by biotite–plagioclase gneiss, sillimanite–garnet–kyanite schist, and small amounts of quartzite, marble, and amphibolites, while the latter is characterized by strongly deformed fine-grained biotite gneiss and biotite–quartz schist (Zhao et al., 2013). The Mesozoic stratigraphy comprises volcanic, subvolcanic, and volcanic-sedimentary rocks, such as rhyolite, tuff, lava, tuffaceous sandstone, and siltstone. From the younger to the older, there are the Chishi Group (K_2ch), the Simaoshan Group (K_1sh), the Bantou Formation (J_3b), the Nanyuan Formation (J_3n), the Changlin Formation (J_3c), the Lishan Formation (J_1l), and the Jiaokeng Formation (T_3j) (Fig. 2).

2.3. Intrusive rocks

The study area contains intrusive rocks having mafic to felsic composition including peridotite, gabbro, syenite, diorite, granite and granite-porphyry. The intrusive rocks are mainly concentrated in the Pucheng-Yangyuan uplift (Fig. 1). The dominant rocks are composed of the Triassic Indosinian and Jurassic-Cretaceous Yanshanian intermediate to acidic intrusive rocks. For example, the Gaoxi granite with an outcrop area of about 100 km^2, locating in the north part of the area intruded in the Mayuan Group (Fig. 2). It is mainly medium-grained biotite granite, dated by zircon U–Pb isochron method to yield a weighted average age of 232 ± 2 Ma (Zhao et al., 2013). The Gaoxi granite underlying Mayangtou deposit consists of comparatively high uranium concentrations (8.52×10^{-6} of the average uranium content) and is considered as source rocks for uranium mineralization (Chen, 1997). Distributed spatially along the NNE–NE–striking faults, the exposed granite batholiths, dykes, and stocks mainly intruded into the Proterozoic metamorphic rocks and Mesozoic volcanic rocks, showing genetic relationship with uranium mineralization (Zhou, 2012).

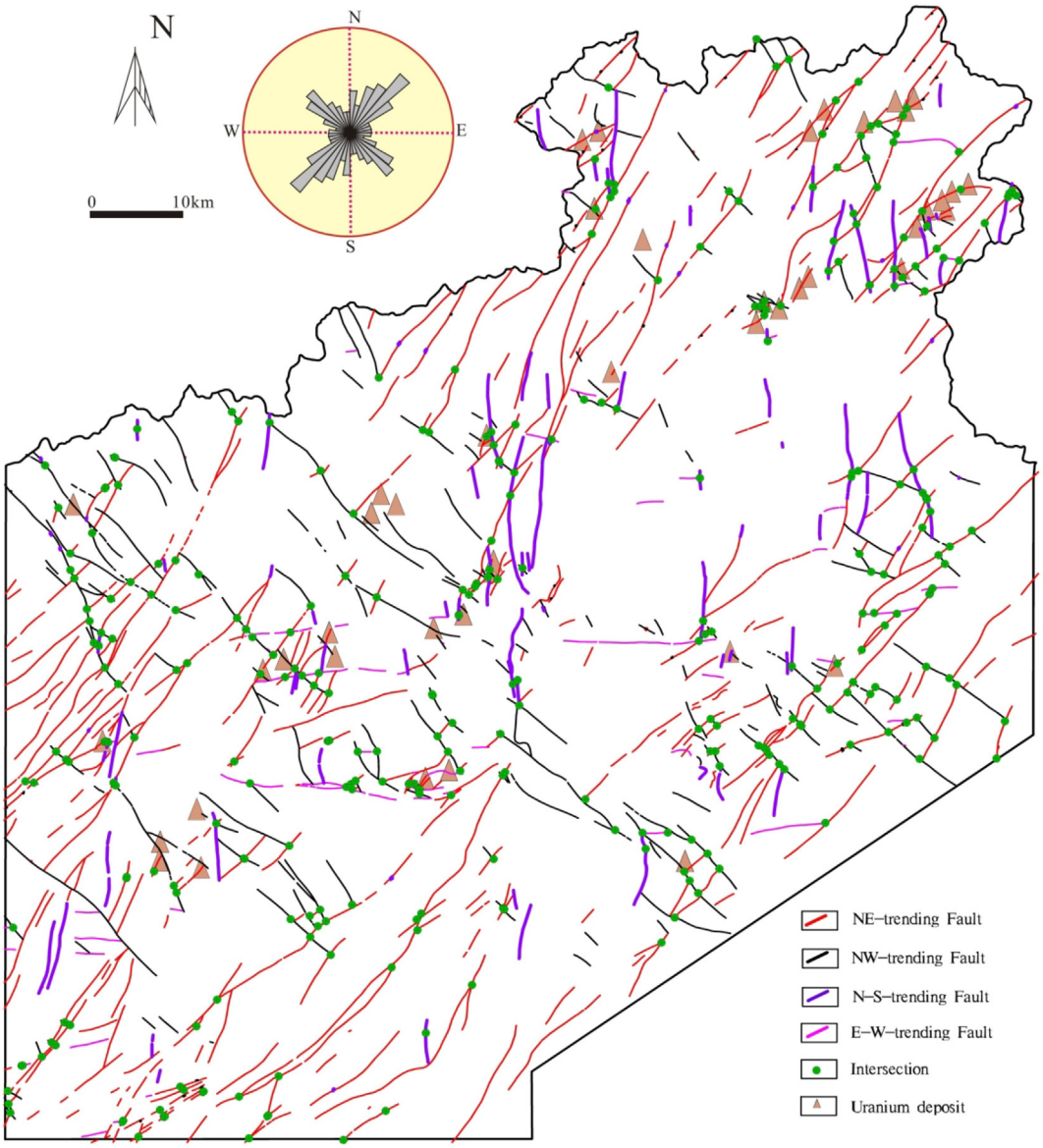

Fig. 3. The distribution of faults in Pucheng district and the rose diagram of faults.

2.4. Structures

A prolonged history of tectonic activity has been recorded for the rocks in this district. The regional NE–striking fault zones, such as Chong'an–Shicheng, Pucheng–Wuping, Nanping–Ninghua, and Zhenghe–Dapu (Fig. 1), not only provide a channel for the rise of tectonic hydrothermal fluids, but also promote uranium migration and enrichment from the host rocks (Zhang, 1986; Huang, 2010; Li et al., 2012). Faults in this district strike NW–SE, NE–SW, E–W, and N–S, and as illustrated by the rose diagram, the major trend of the fault systems are NE–SW and NW–SE, which cut different lithological units (Fig. 3). The NE–SW faults concentrated in the volcanic rocks area situated in the western region, probably belong to the structural traces in the Jurassic–Cretaceous Yanshanian period. These faults, having 60–80° dip angles, are mainly characterized by compression or tension-torsional properties, indicating multiple episodes of activities (Zhou, 2012). The NW-SE faults mainly exhibit normal dip-slip displacements; and these faults are widely distributed in the central and eastern parts of the area.

3. Uranium mineralization characteristics and conceptual genetic model

The Pucheng district is located within the Wuyishan metallogenic belt. This district witnessed strong tectonic activity and large-scale magmatism. Consequently, not only the sources of metallogenic materials are present for mineralization, but also the heat sources for the activation and enrichment of the metallogenic elements are provided (Zhou, 2012). The district contains abundant Mesozoic granites and volcanics, as well as tungsten–molybdenum, niobium–tantalum, rare earth elements and uranium deposits. A number of uranium deposits and mineralization occurrences have been observed in this area. Major deposits include the Maoyangtou, Shiyuanlong and Quezishan uranium deposits shown in Fig. 2, which have approximately 2000 t, 800 t, and 600 t of uranium reserves, respectively; and the grades averaged 0.185%, 0.276% and 0.103%, respectively (Zhou, 2012). Till date, 46 uranium deposits and mineral occurrences have been discovered in this region, with total combined uranium reserves of more than 4000 tons. Notable, the genesis of uranium mineralization is closely related to volcanic activity in the Late Mesozoic that favored mineral enrichment. The volcanic-type uranium mineralization shows great potential and

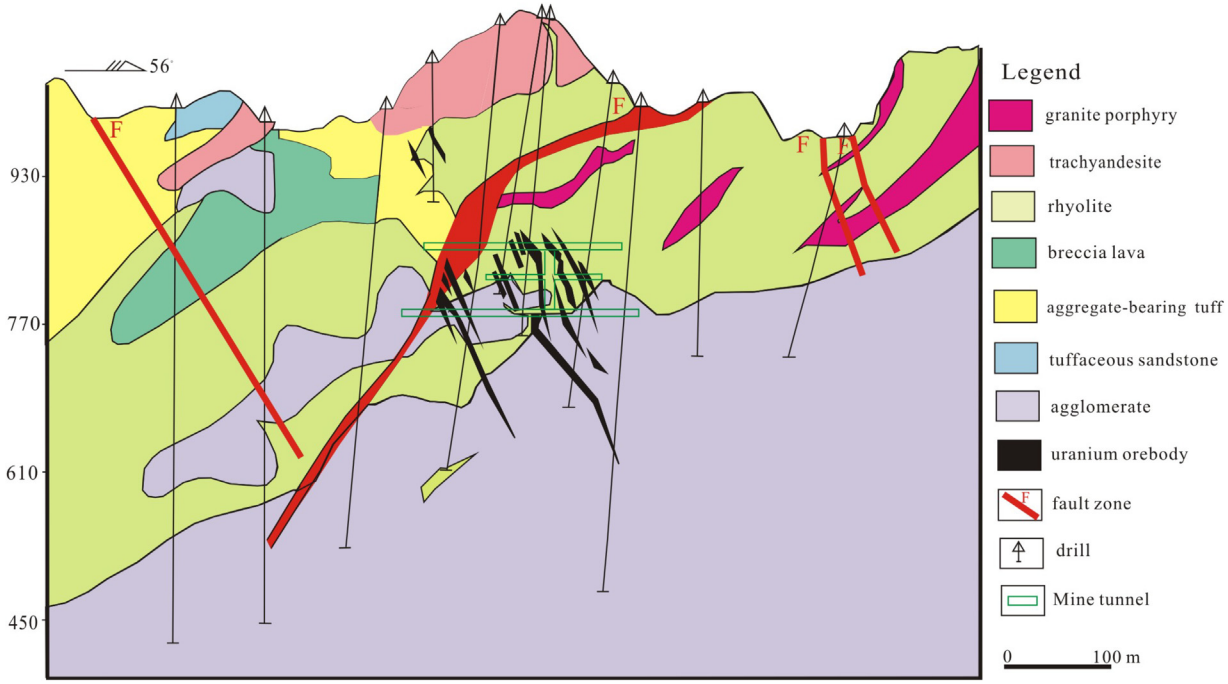

Fig. 4. The exploration section of Maoyangtou deposit (modified from the study of Zhou, 2010).

Table 1
Summary of characteristics of major uranium deposits discovered in the Pucheng district of China. Data are sourced from Lu and Wang (1990), Chen et al. (1995, 1997), Lu et al. (1997), Zhou (2010, 2012), and Lou (2013).

Uranium deposits	Maoyangtou	Quezishan	Shiyuanlong
Host rocks	Rhyolite (J_3n), granite porphyry	Rhyolitic tuff and ignimbrite(J_3n)	Rhyolitic tuff(J_3n)
Ore-controlling structure	NE-striking faults, followed by NW-striking faults	NW- and NNE-striking faults	NW- and NNE-striking faults
Ore minerals	Pitchblende, coffinite, hematite, brannerite limonite, molybdenum,	Pitchblende, coffinite, hematite, pyrite, galena, sphalerite, limonite	Pitchblende, coffinite,hematite, pyrite, limonite
Gangue minerals	Quartz, fluorite, Hydromica, Clay Minerals	Quartz, chalcedony, hydromica, kaolin, etc.	Quartz, fluorite, calcite,hydromica, etc.
Wall-rock alteration	albitization hydromicazation; silicification, chloritization, hematization, pyritization	chloritization, hydromicazation silicification, chloritization,carbonation, pyritization	Hematitization, chloritization,fluoritization, silicification,sericitization, pyritization,
Orebody shape	vein, stockwork, lenticular	bedded, stratoid, lenticular	bedded, lenticular
Metal element association	U, Mo, Ag	U, Mo	U, Cu, Au
Grade/tonnage	0.185%/2276 t	0.101%/602 t	0.276%/805 t
Mineralization Temperature (°C)	140–180	170–220	–
Mineralization age (Ma)	89.3–107.7 (Pitchblende of U-Pb age)	–	92–115 (Pitchblende of U-Pb age)

good prospect development for uranium mineral resources in this district. The major host volcanic or subvolcanic rocks belong to the Later Jurassic Nanyuan Formation, which includes a series of continental intermediate and intermediate acid lavas and pyroclastic rocks. The mineralized bodies, appearing as vein, lenticular, and stratiform shapes, are often discontinuous and parallel to the ore-controlling faults. Processes involved in the hydrothermal alteration of the host rocks include hematization, pyritization, silicification, chloritization, sericitization, carbonation, albitization, and hydromicazation. Noteworthy, hematization, albitization, silicification and pyritization alterations are closely related to uranium mineralization, and are well developed in proximity to the mineralized zones (Nie et al., 1994; Zhou, 2010; Lou, 2013). The granitic rocks close to the orebodies also exhibit slight chloritization and silicification alterations. Moreover, Pitchblende and coffinite are crucial ore minerals in uranium deposits. The gangue minerals include quartz, fluorite, hydromica, clay minerals, and a small amount of chlorite and carbonate.

Fig. 4 depicts the exploration section of Maoyangtou deposit. Table 1 summarizes the main characteristics of three major uranium deposits currently known in this area. Accordingly, the conceptual genetic model comprehensively describes the characteristics of uranium ore in this district as follows: (1) uranium deposits and occurrences are observed in various volcanic environments, some are in or directly adjacent to calderas or rhyolite dome (e.g. Maoyangtou deposit), others are observed in outflow rhyolitic tuff distant from source calderas (e.g. Quezishan deposit) (Fig. 2); (2) homogenization temperatures of fluid inclusions are between 140 °C and 260 °C (Chen et al., 1995), indicating that probably the ore-forming fluids are meso– and epithermal. Most of the U-Pb isotope ages of pitchblende fall in a span of 86.8–107.7 Ma, thus the genesis of the ore deposit probably belongs to post-volcanic hydrothermal deposits in Cretaceous (Wang et al., 1990; Chen, 1997); (3) the Mesozoic acid volcanic constitute a primary uranium source for forming an economic deposit. Among the volcanics, rhyolites (9–12 $\times 10^{-6}$ of uranium content) provide an ideal source, followed by rhyolitic tuffs (6–10 $\times 10^{-6}$ of uranium content), and ignimbrites (5–7.5 $\times 10^{-6}$ of uranium content), etc. The uranium-bearing volcanics are chemically characterized by aluminum supersaturated and rich in silica, alkali, and potassium; (4) the granitic rocks, in particular, the

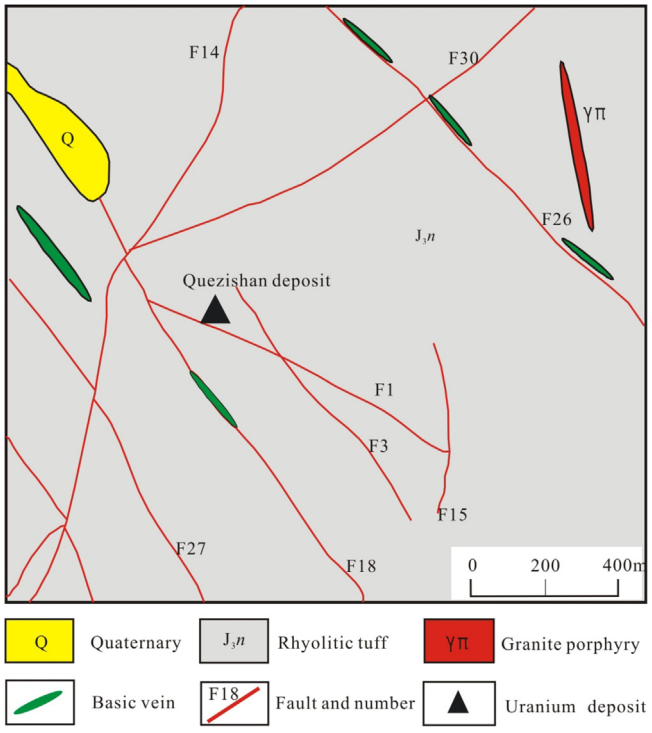

Fig.5. Simplified geological map of Quezishan uranium deposit showing the ore-controlling characteristics of faults (modified from Lou, 2013).

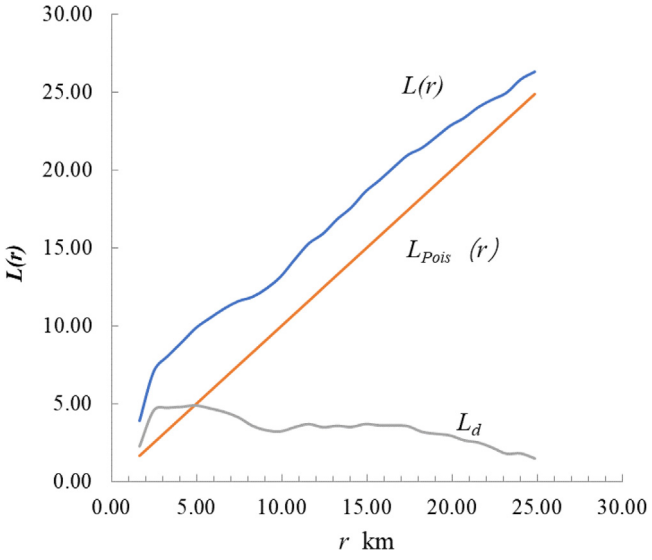

Fig. 6. Plot of L(r) versus r for uranium deposits.

granite porphyry (9–16 × 10^{-6} of uranium content), can been considered as a potential heat and fluid source to contribute significant quantities of uranium. Nie et al. (1994) reported that the uranium mineralization in the granite porphyries and volcanics exhibited the same mineralization system. Based on the isotope analysis, Chen (1997) proposed that the uranium in Maoyangtou deposit was probably derived mainly from volcanic and subvolcanic in the early stage, and leached from granite in the late stage. The superposition of multi-stage and multiple mineralization favors the formation of economical uranium deposits; and (5) The NE– and NW–striking faults, as well as the intersection of a fault and a lithological/intrusive contact, have resulted in the formation of a zone of weakness to control the transportation and carry large uranium resources. For example, the Quezishan deposit is mainly controlled by NNE-striking faults and NW-striking faults

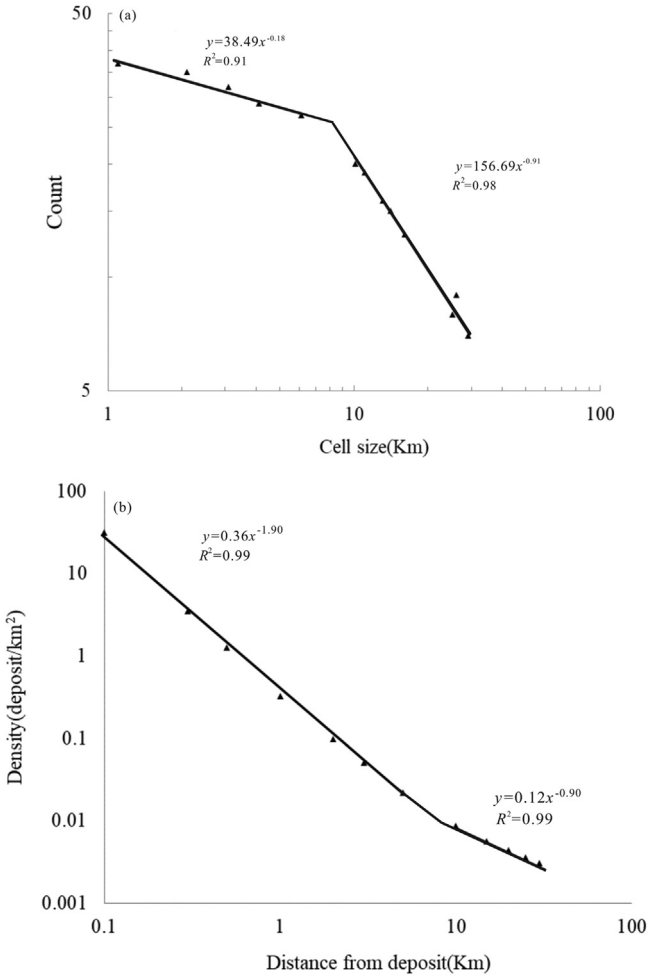

Fig. 7. Log-log plots of (a) box size vs. counts, and (b) distance vs. the density of ore deposits.

(Fig. 5), while Maoyangtou deposit is jointly controlled by NE- and NW-striking fault zones adjacent to the south of volcanic conduit (Zhou, 2012).

4. Methods and dataset

4.1. Fractal models

Fractal models can efficiently characterize complex geological processes. The fractal dimension is often obtained by the box-counting technique (Velde et al., 1990; Carlson, 1991; Turcotte, 1992; Walsh and Watterson, 1993; Blenkinsop and Sanderson, 1999; Pérez-López et al., 2005; Zuo et al., 2009b; Zhao et al, 2011; Zuo, 2016; Zuo and Carranza, 2017). First, a group of cells with different cell sizes r was used to cover the point (e.g. ore deposit or structural intersection) or lineament (e.g. fault or geologic boundary) maps, and the number of cells $N(r)$ occupied by points or lineaments was counted. Second, the data pairs for cell size r and number $N(r)$ were plotted on a log-log graph and linear regression was applied to fit a straight line from which the box dimension D_b could be estimated (Carlson, 1991; Raines, 2008; Carranza, 2009; Zuo et al., 2009b). This relationship can be expressed as follows:

$$N(r) = kr^{D_b-2} \quad (1)$$

where r is the measure of cell size. $N(r)$ denotes the cumulative number of cells containing one or more lineaments or points, D_b represents the box-counting fractal dimension, and k is a constant. D_b can be obtained from the slope coefficient of the linear regression between the dataset of

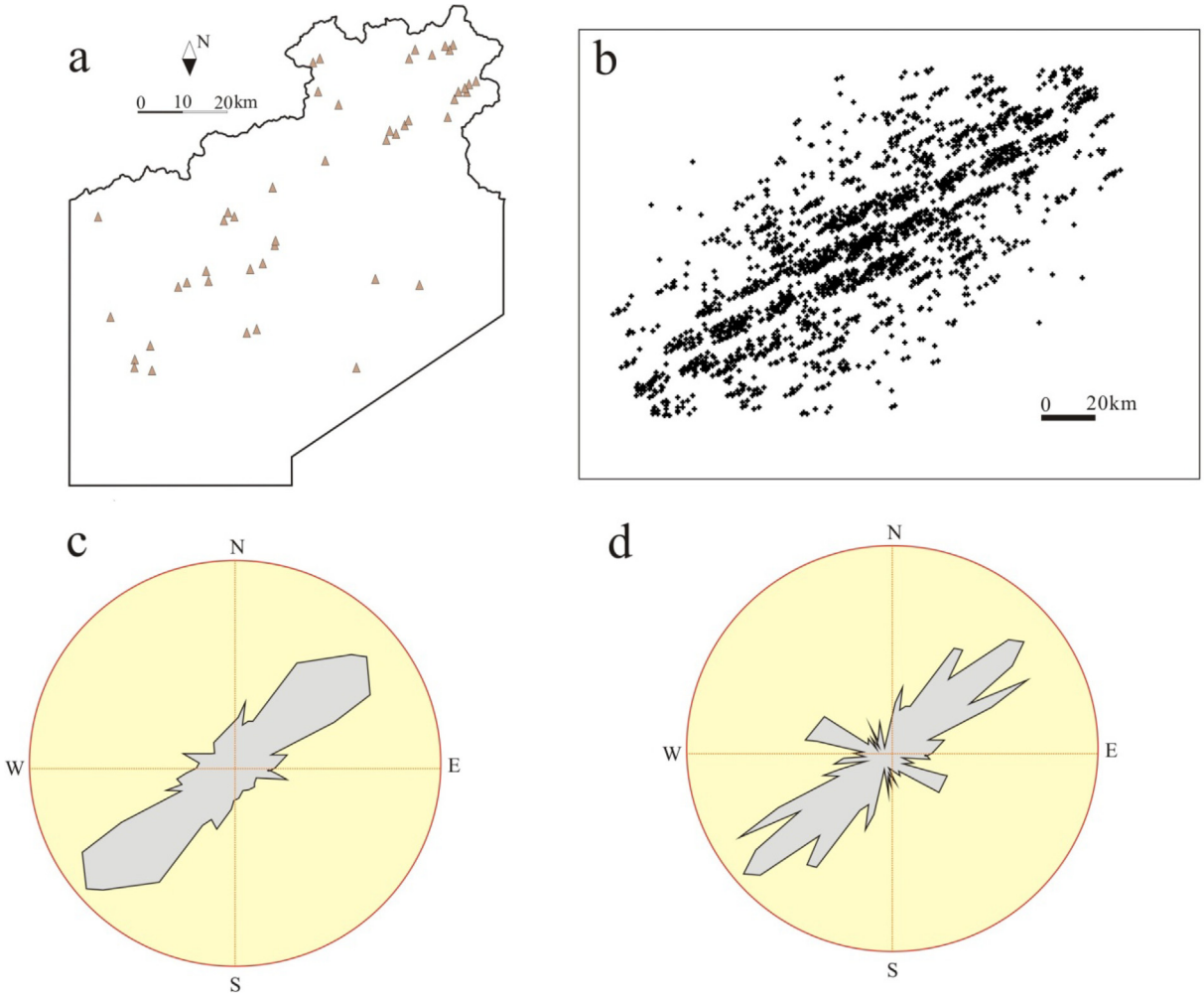

Fig. 8. Results of Fry analysis for uranium deposits: (a) the spatial distribution of mineral deposits, (b) Fry plot, (c) the rose diagram of all pairs of Fry points, and (d) the rose diagram of pairs of Fry points < 8 km.

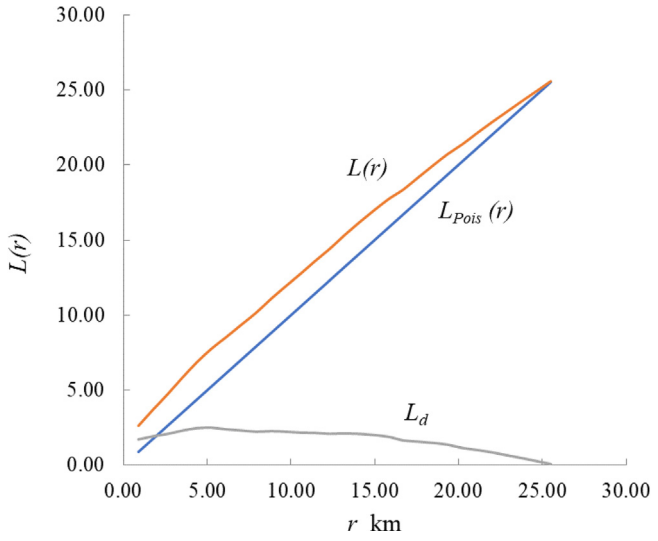

Fig. 9. Plot of L(*r*) versus *r* for fault intersections.

N(*r*) and *r*. Mandelbrot (1983) also showed that fractal point patterns satisfied a radial-density power-law relation, thus:

$$d = C\delta^{Dr-2} \quad (2)$$

where *d* is the density of the points, D_r is the radial-density fractal dimension (also called cluster dimension), and *C* is a constant.

4.2. L function

The point patterns can be characterized by three types, which are Poisson process, regularity and clustering; in these types, the points are randomly distributed, tend to avoid each other, and tend to occur together, respectively (Diggle, 1983; Carranza, 2009; Zuo et al., 2009b; Wang et al., 2015). The *L*(*r*) function can be used to judge whether a point pattern satisfies the Poisson distribution. It can be expressed as follows (Baddeley and Turner, 2005; Zuo et al, 2009b):

$$L(r) = \sqrt{\frac{K(r)}{\pi}} \quad (3)$$

where *K*(*r*) can be estimated by using the empirical cumulative distribution function of pairwise distances between all distinct pairs of the points x_i and x_j ($i \neq j$) in the point pattern (Ripley, 1977)

$$K(r) = \frac{1}{\lambda^2 A} \sum_i \sum_{j \neq i} w_{ij}^{-1} \{\|x_i - x_j\| \leq r\} \quad (4)$$

where *A* represents the area of the studied region, λ represents the intensity (the ratio of the total number of mineral deposits to *A*), and w_{ij} denotes the proportion of the circumference of the circle around the point *i* with radius *r* that lies within *A*. The *L*(*r*) function can be used to determine if a point pattern is randomly distributed (L(*r*) = *r*), or exhibits clustering (L(*r*) > *r*), or regularity (L(*r*) < *r*).

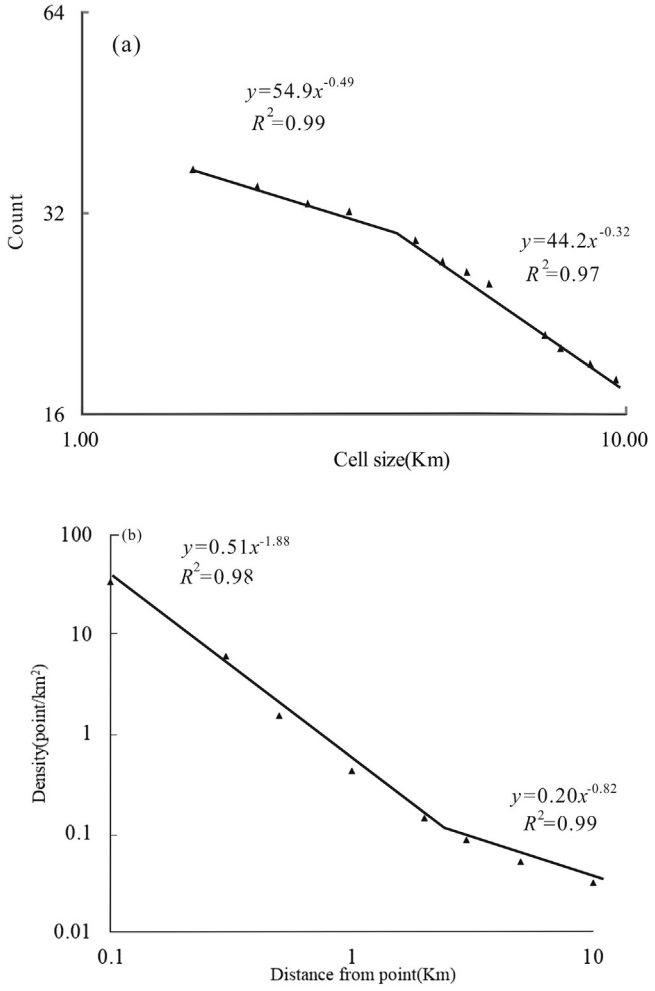

Fig. 10. Log-log plots of (a) box size versus counts, and (b) distance versus density of fault intersections.

4.3. Fry analysis

Fry analysis (Fry, 1979) is a geometrical method involving spatial autocorrelation analysis for points. Fry method, which plots translations of a set of points, can be performed by the following procedures (Vearncombe & Vearncombe, 1999; Carranza, 2009; Zuo et al., 2009b; Parsa and Maghsoudi, 2018). First, a map of points is marked with a series of parallel reference lines. Then in a second empty map, the intersection of an N-S line and an E-W trending line can be taken as the origin, which is then placed on top of one of the points. In this step, it is necessary to ensure that the reference lines for the same direction are kept parallel and that the positions of all the points are recorded in the second map. The procedure continues until all the points have been used as the origin on the overlay map. Fry plots can be used for visual interpretation for providing insight into which geological features are plausible geological controls (Vearncombe & Vearncombe, 1999; Kreuzer et al., 2007; Carranza, 2009; Zuo et al., 2009b).

4.4. Artificial neural network

The ANNs are reliable pattern-recognition and classification tools that can be generalized from imprecise input data (Bonham-Carter, 1994; Müller et al., 1995). The ANNs have two major components including neurons and connections, which are a set of weighted interconnections among processing units (Huang and Williamson, 1996; Leite et al., 2009). The back-propagation ANN (BP-ANN) contains forward and backward computation processes and comprises of input, output and at least one hidden layer. The neurons of the hidden and output layers process their inputs, sum the product(s), and then process the sum(s) using a log-sigmoid transfer function. The learning algorithm can automatically minimize the error by tuning a corresponding weight to generalize and predicts outputs from the inputs (Thompson et al., 2001).

4.5. Dataset

The datasets, consisting of geological and airborne radioactive survey data in this study, were obtained from the 294th Geological Party of Fujian Nuclear Industry of China. The geological dataset contains a 1:100,000 geological map including volcanic rock formations, intrusive rocks, faults, and mineral occurrences. The airborne radioactive survey data contain anomaly maps of K, Th, γ, and U.

5. Results

5.1. Spatial pattern analysis of uranium deposits

Plots of r versus $L(r)$ (Fig. 6) indicate that 46 known uranium deposits are clustered because of the $L(r)$ values being greater than those of the Poisson patterns ($L_{Pois}(r)$). The L_d value, representing the difference between $L(r)$ and $L_{Pois}(r)$, is used to indicate the degree of clustering. Uranium deposits acquired the highest degree of clustering (L_d = 4.8) when r was 5 km. Fractal plots indicate that the spatial patterns of the deposits appear to be bifractal with two box-counting fractal dimensions (D_b) (D_b = 0.18, r < 8 km; D_b = 0.91, r > 8 km, referring to the local dimension and regional dimension, respectively) (Fig. 7a), andl two radial-density fractal dimensions (Dr) (D_r = 0.10, r < 8 km; D_r = 1.10, r > 8 km))(Fig. 7b). Fry plots were constructed with all pairs of Fry points and with pairs of Fry points within 8 km by using the freeware DotProc package (Fig. 8). The results clearly demonstrate a dominant regional NE orientation (Fig. 8c). The rose diagram of pairs of Fry points within 8 km shows a subsidiary NW orientation (Fig. 8d).

5.2. Spatial pattern analysis of intersections of faults

The 326 intersections were derived from the fault map. Plots of r versus $L(r)$ indicate that the intersections are clustered (Fig. 9). The L_d value shows that the highest degree of clustering occurs at r = 5 km (L_d = 2.5). Fractal analysis demonstrates bifractal distributions according to log–log plots (Fig. 10). Box-counting fractal dimensions (D_b) are 0.49 (r < 5 km) and 0.32 (r > 5 km); and radial-density fractal dimensions (Dr) are 0.12 (δ < 5 km) and 1.18 (δ > 5 km). Fry plots, constructed with all pairs of Fry points and with pairs of Fry points within 5 km, present a dominant regional NE orientation and prospect-scale NW- and NE-trending faults similar to the mineral occurrence (Fig. 11).

5.3. Fractal dimensions of lineament structures

Fractal dimensions of the lineament structures (faults and lithological boundaries) were calculated on a 2 km grid of cells of the entire study area (considering the map scale and the distribution of the structures). The spatial resolutions were 1000, 500, 400, and 200 m, respectively. The parameters such as frequency (Lf), lengths (Ll) and number of intersection (Li) of lineament structures were also obtained by statistical methods, which exhibited positive correlations with fractal dimension (Table 2). Accordingly, fractal dimension can be used as an index to define the complexity of lineaments, as well as the density and interconnectivity of fluid pathways to some extent. Fig. 12 exhibits the maps of the fractal dimensions achieved by interpolation. The highest areas are spatially associated with the faults and lithological contacts that have developed well in the volcanic rocks.

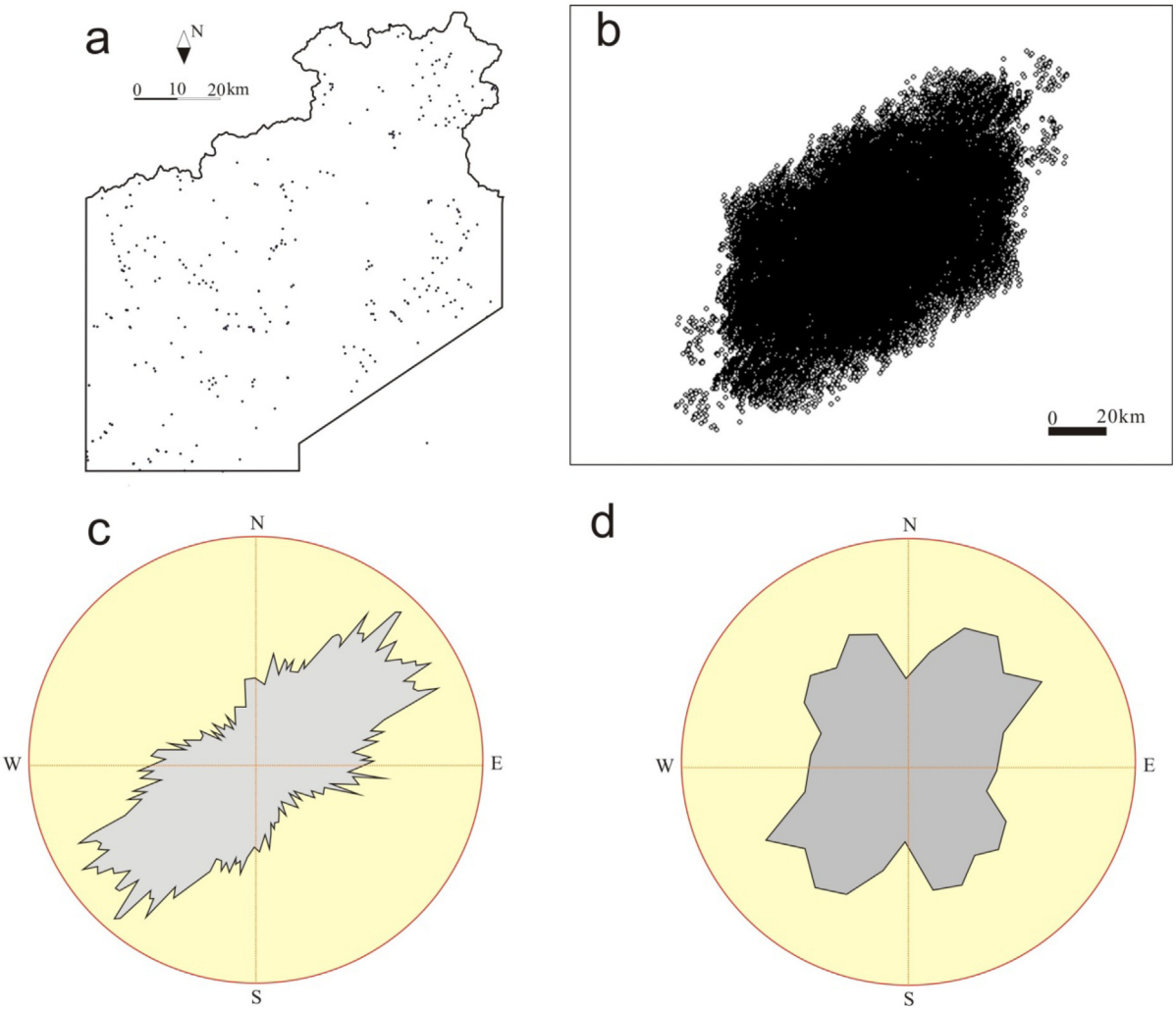

Fig. 11. Fry analysis for fault intersections:(a) the original points, (b) the Fry plot, (c) the rose diagram of all pairs of Fry points, and (d) the rose diagram of pairs of Fry points < 5 km.

Table 2
Coefficient matrix of length, intersection, frequency and dimension.

	length	Intersection	Dimension
Frequency	0.52	0.61	0.63
Length		0.32	0.59
Intersection			0.44

6. Discussions

6.1. Complexity of spatial distribution of structures and locations of uranium deposits

Previous studies and the conceptual genetic model of uranium mineral systems have shown that the uranium deposits are structurally controlled in this district (Huang, 2010; Li et al., 2012; Zhou, 2012). The faults, lithological interfaces of strata, and volcanic structures are the dominant permeable fluid pathways that control the location of deposits in uranium mineral systems. These structures can provide the pathways for this focused fluid flow on one hand, and create contrasts in physico-chemical conditions by juxtaposing different rock types on the other (Hodkiewiczi et al., 2005; Ford and Blenkinsop, 2008). Fig. 12 demonstrates that the fractal dimension of lineaments was determined to indicate the possibility of a correlation between the complexity and the size of deposits. Clearly, the highest areas are spatially coincident with the spatial distribution of ore occurrences. The high-tonnage deposits, such as the Quezishan, Maoyantou, and Shiyuanlong deposits, also exhibit a high correlation with geological complexity. Furthermore, in order to examine this relationship spatially, the correlations between fractal dimensions, and ore occurrences and tonnages, are shown in Fig. 13. The positive correlations reflect that areas of greater complexity have the potential to be richer in ores. This may be attributed to the fact that hydrothermal mineral systems often develop into structures having sufficient connectivity to create fluid-pathway networks. The latter links fluid sources and favors the formation of ore deposits (Cox et al., 2001; Hodkiewiczi et al., 2005). Higher complexity of the surface structures indicates well-connected and high-permeability fracture networks at depth. These networks act as pathways to focus hydrothermal fluids to form ores (Hodkiewiczi et al., 2005; Zhao et al., 2011). Greater complexity, characterized by larger fractal dimensions, implies the potential zones where large tonnage deposits may have formed.

6.2. Spatial association of uranium deposits with faults

The results obtained by Fry, fractal, and *L* function analyses are presented in Table 3. The results of the two fractal analysis methods for uranium deposits are similar in separating the straight lines fitted through log-log plots at an 8 km scale. This implies that certain types of geological control on the clustering of uranium occurrences might be

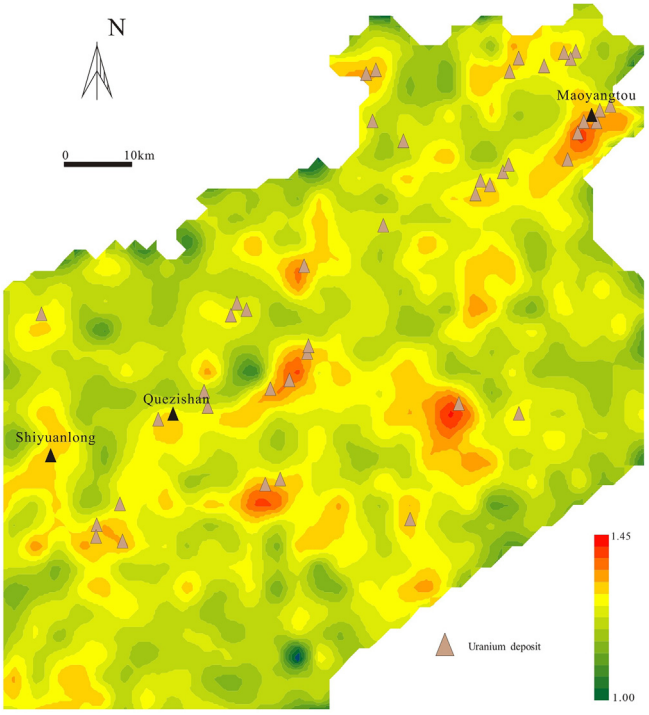

Fig. 12. Maps showing the fractal dimension of faults and lithological boundaries.

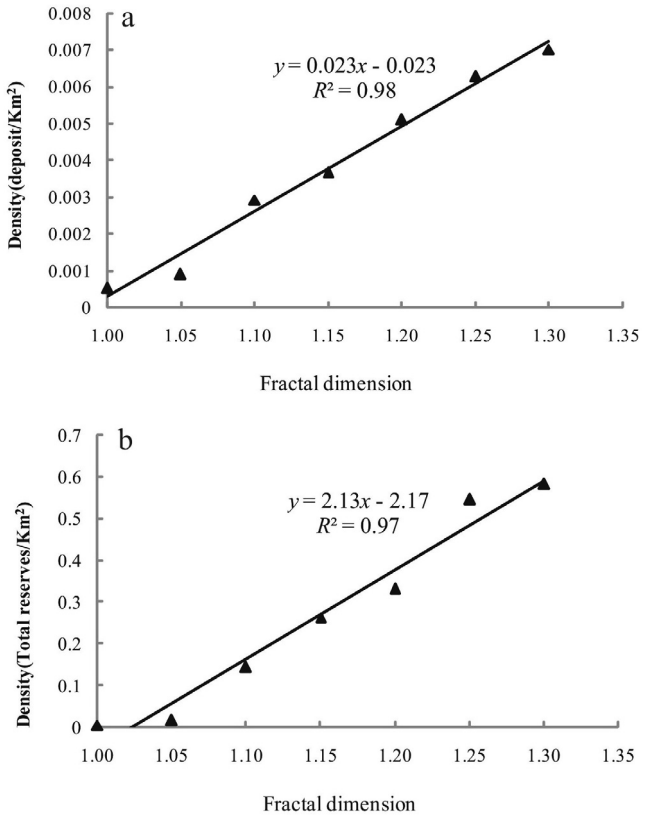

Fig. 13. Plots of the fractal dimensions versus (a) density of mineral deposits, and (b) density of ore reserve.

carried out through regional- and prospect-scale processes that plausibly controlled their formation. Carlson (1991), Carranza (2009) and Zuo et al. (2009b) proposed that the first range might represent the extent of a hydrothermal mineralization system; and the second range represented the influence distance for regional geological background. These interpretations were further investigated by the application of Fry analysis. The rose diagrams of Fry analysis suggest a major 30°–60° orientation with all pairs of Fry points and two dominant 30°–60° and 290°–310° orientations with pairs of Fry points within 8 km, respectively. These results of the Fry analysis not only cohere with those of fractal analysis, but also indicate a spatial and possible genetic link between the location of uranium deposits and regional-scale NE-, prospect-scale NE-, and NW-striking faults. Fry plots of uranium occurrences constrained by ore tonnage (T) further provide insights into structural controls on uranium deposits (Fig. 14). They suggest a major NE–striking orientation and two dominant NE– and NW–striking orientations within 10 km for larger deposits ($T > 10$ t), and NE–striking orientation and three dominant NE–, NEE–, and NW–striking orientations within 10 km for smaller deposits ($T < 10$ t). Such results coincide well with the results from the study of Zhou (2012) and Lou (2013), which concluded that the faults, such as regional NE–striking Chong'an-Shicheng, Pucheng–Wuping fault zones (Fig. 1), NE–striking F14, F30 faults, and NW–striking F1, F3, F18 in Quezishan deposit (Fig. 3), are likely to have controlled the uranium mineralization in the Pucheng district.

The intersections of faults were also used to form an important set of points in order to analyze the structural controls; indeed, the areas surrounding the fault intersections with higher permeability can be appropriate for the penetration of ore-forming fluids that subsequently lead to mineralization (Zhao et al., 2015). Table 3 presents that the similarities between the spatial distribution of mineral occurrences and the intersections of faults were also observed (Table 3). Results of the two fractal analysis methods are similar in separating the straight lines at 5 km compared to that at 8 km for mineral occurrences. The local box dimension of intersections is larger than ore occurrences. These results may be attributed to the higher intensity of intersections. Zuo et al. (2009b) illustrated the fractal dimension to be a function of intensity and probability of distance, and a higher intensity point pattern generally has a larger box dimension. Fry analysis also showed the regularity similar to ore occurrences, displaying regional- and prospect-scale controls on the distribution of intersections. Quantification of the spatial association of NE-, NW-, E-W-, and N-S-striking faults (Fig. 3), as well as intersections of faults with uranium deposits further support the preceding idea (Fig. 15). The results clearly indicate that the ore-bearing fluids might have been dominantly transported through NE-, and NW-trending fault pathways. The intersections of faults with lager permeability and connectivity promote the migration and focusing of ore-bearing fluid; which consequently leads to the formation of ore deposits.

6.3. Lithological controls on uranium mineralization

Most of the uranium mineralization in Pucheng district originated from volcanic rocks of the Later Jurassic Nanyuan Formation, while some originated from both volcanic and intrusive rocks (Zhou 2010; Li et al., 2012). The conceptual genetic model indicates that the volcanic and intrusive rocks constitute significant metal resources for forming an economic uranium deposit. Fig. 16 shows the significance of spatial association between these rock units and uranium mineralization, characterized by the number of ore deposits, and uranium content. The results revealed the existence of strong positive spatial associations between the Nanyuan formation and granite with uranium occurrences. Therefore, these rock units might be the plausible lithological control concerning uranium mineralization.

6.4. Mapping uranium prospectivity

MPM involves geological/geochemical/geophysical features associated with the targeted mineral deposits. These features, termed as exploration criteria, are spatial signatures of critical processes in the

Table 3
Comparison of the uranium deposits and intersections of faults by Fry analysis, fractal analysis and *L* function.

Method	Uranium deposits (No.46)	Intersections of faults (No.326)
L-function	$L(r) > L_{pois}(r)$, clustering highest L_d value = 5 km(r = 5 km)	$L(r) > L_{pois}(r)$, clustering highest L_d value = 2.5 km(r = 5 km)
Fractal analysis	D_b = 0.18(r < 8 km); D_b = 0.91(r > 8 km) Dr = 0.10(δ < 8 km) ; Dr = 1.10(δ > 8 km).	D_b = 0.49(r < 5 km); D_b = 0.32(r > 5 km) Dr = 0.12(δ < 5 km) ; Dr = 1.18(δ > 5 km).
Fry analysis	prospect-scale controls: dominate NE-trending faults, subsidiary NW-trending faults regional-scale controls: dominate NE-trending faults	prospect-scale controls: dominate NE- and NW-trending faults regional-scale controls: dominate NE-trending faults

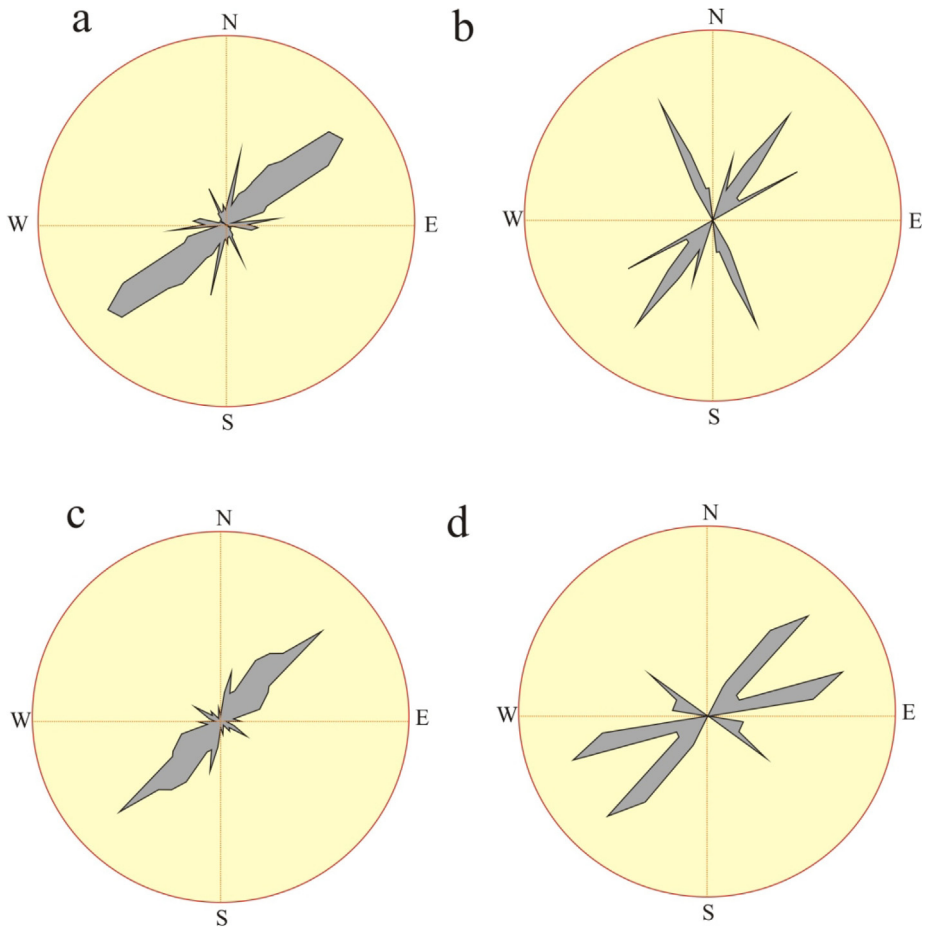

Fig. 14. Fry plots of uranium deposits constrained by ore tonnage. (a) and (b) represent the rose diagram of all pairs of Fry points and pairs of Fry points within 10 km for the larger deposits (> 10 t); (c) and (d) represent the rose diagram of all pairs of Fry points and pairs of Fry points within 10 km for the smaller deposits (< 10 t).

mineral systems (McCuaig et al., 2010; Fallon et al., 2010). In uranium mineral system, three groups of factors are considered to be essential, which are uranium source, pathway of ore-forming fluids, and favorable physico–chemical conditions for uranium deposition and preservation (Xiao and Wang, 1998; Kreuzer et al., 2010; Nash, 2010; Porwal et al., 2015; Hou et al., 2017). The exploration criteria can be inferred from various geoscience datasets to extract criteria in the form of evidential layers. Based on the preceding analysis of the conceptual genetic model and controls on the uranium mineralization, nine exploration targeting criteria (L1 ~ L9) for volcanic-type uranium systems that can be mapped in the available data sets, were summarized for integrated prospectivity modeling (Table 4). These criteria included the Nanyuan Formation, granite, fractal dimension anomaly (> 1.15), NE- and NW-striking faults, intersections of faults, calderas airborne radioactive uranium (U) anomaly (> 6 ppm), and airborne radioactive gamma (γ) anomaly (> 3.1 nc/kg.h). The buffer radii of 1.0, 1.2, 2.0 and 5 km were considered according to the areas containing approximately 75% of known deposits. Airborne radioactive U and γanomalies are important geophysical exploration criteria in uranium mineral exploration, providing results about the uranium deposition and preservation (Nash, 2010). The anomaly maps clearly indicated that the anomalies are mainly concentrated in the north and the west parts, which coincide with the distribution of uranium-rich volcanic rocks (Fig. 17). The thresholds were selected according to the background values in this area (Zhou, 2012).

The unit cell size for GIS-based prospectivity analysis depends on the size of the deposits and the geological data input (Hengl, 2006). In this study, 2 km × 2 km unit cells were used in the predictive modeling. These cells were objectively determined based on the spatial pattern of the known uranium deposits, so that they were suitable to the scale of the analysis, and that only one occurrence was present in any given cell (Carranza and Laborte, 2015). Then, the BP-ANN method was used to create probability maps for uranium occurrences, which involves the following procedures (Zhao et al., 2016):

(1) Training and validation set construction. The training and

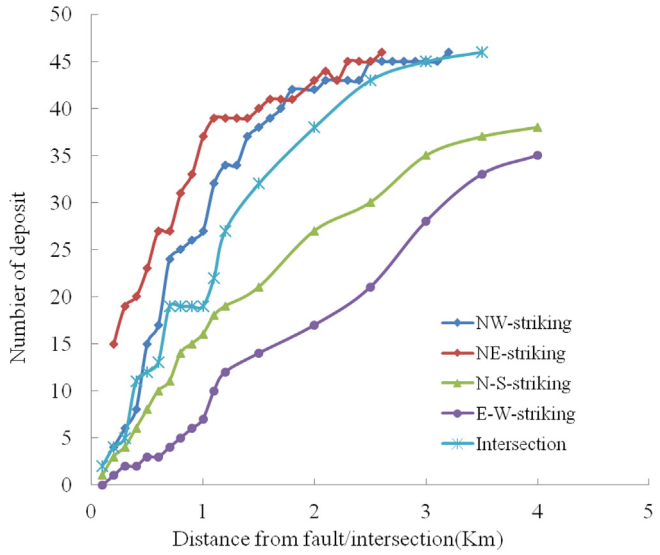

Fig. 15. Plot of distances versus uranium deposits for different fault groups.

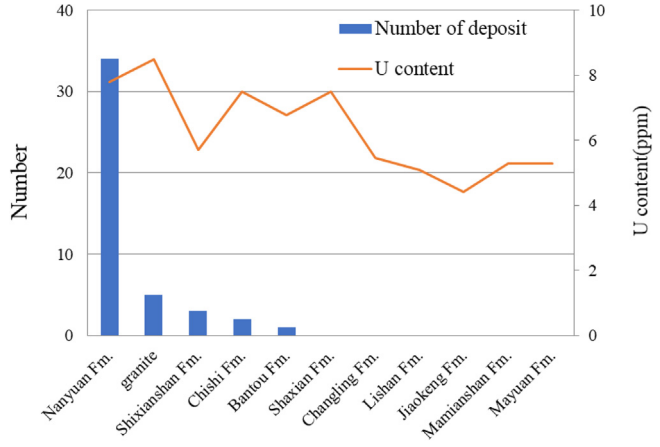

Fig. 16. Plot of rock units versus uranium deposit and content.

validation patterns including both positive (presence) and negative (absence) patterns were created. The 46 known mineral deposits units were randomly split between training/validation (70/30). An equal number of none-deposit units were randomly selected for training and validation units. None-deposit units should be far from the deposit locations with the objective of having their geological characteristics different from those of the deposits (Parsa et al., 2018). In this research, the none-deposit units were selected in the area where the distances from known deposit were greater than 5 km, as a result of the *L*-function results of uranium deposit. The locations of the selected training units, validation units for the ANN

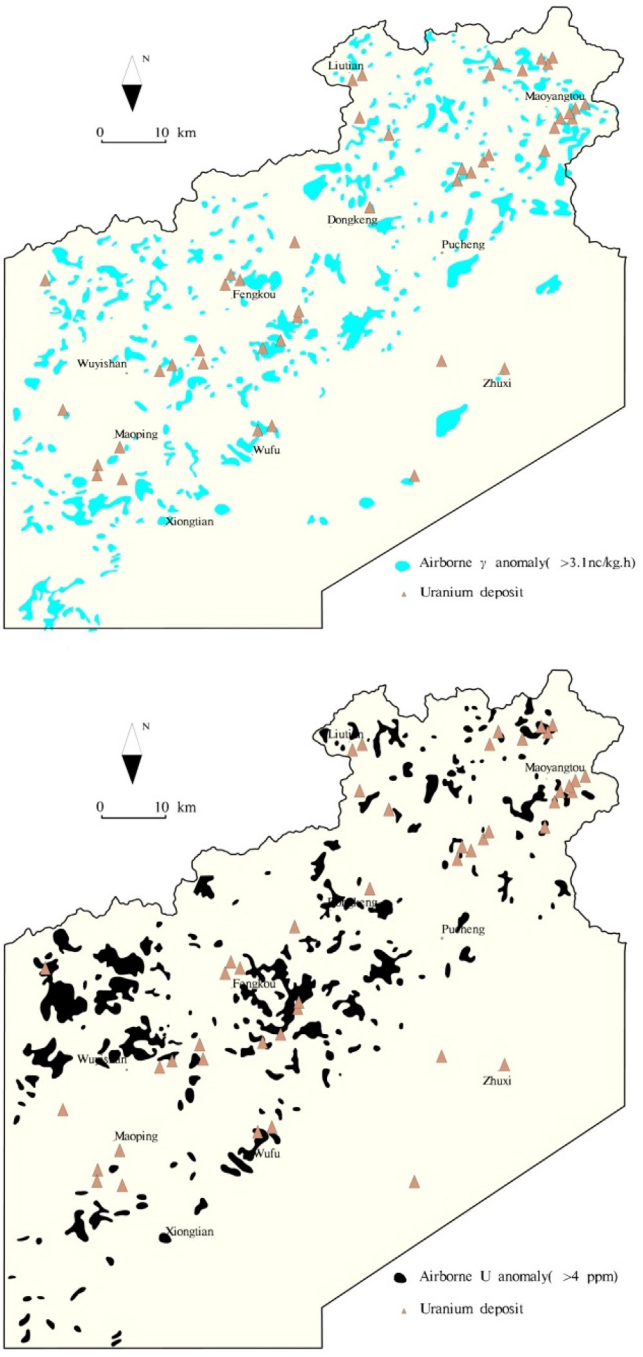

Fig. 17. Maps showing (a) airborne radioactive U and (b) airborne radioactive gamma.

Table 4
. The exploration targeting criteria for volcanic-type uranium systems.

Targeting criteria	Evidence layer	Description	Buffer (km)	AUC
Sources	Uranium-rich strata (L1)	Presence of or proximity to the Nanyuan Fm.		0.824
	Uranium-rich intrusion (L2)	Presence of or proximity to the granite		0.525
Pathways	NE-striking faults (L3)	Presence of the buffering zones of NE-striking faults	1	0.766
	NW-striking faults (L4)	Presence of the buffering zones of NW-striking faults	1.2	0.712
	Intersections of faults (L5)	Presence of the buffering zones of intersections	2	0.669
Traps	Volcanic environments (L6)	Presence of the buffering zones of calderas	5	0.663
	Lineament complexity (L7)	Presence of fractal dimension anomaly (D > 1.15)		0.796
Deposition	Airborne radioactive gamma (γ) anomaly (L8)	Presence of γ anomaly((> 3.1 nc/kg.h))		0.742
	Airborne radioactive uranium (U) anomaly (L9)	Presence of U anomaly(> 6 ppm)		0.630

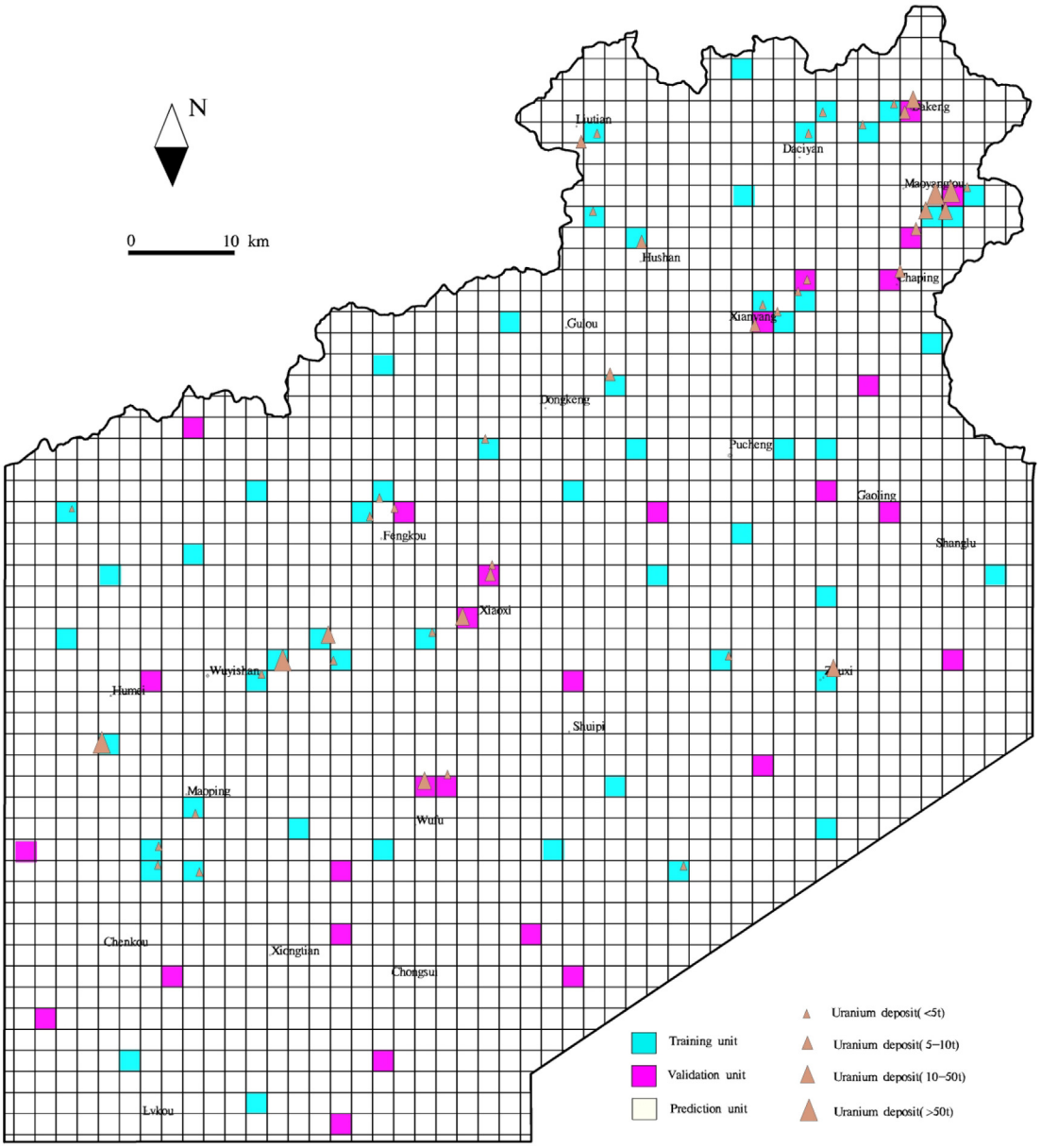

Fig. 18. Locations of the selected training and validation units for the ANN.

are shown in Fig. 18.

(2) The BP-ANN model implementation. Nine variables were used as inputs, and all input variables were transformed into [0, 1] by normalization. The number of the hidden neurons (N_{hid}) was determined by using an empirical formula expressed as $N_{hid} = \sqrt{mn}$, where m and n represent the input and output neurons, respectively (Shen et al., 2008). Then, one hidden layer with six neurons was used for training. The number of inputted neurons corresponded to the nine evidential layers. The output layer considered the sizes of the uranium deposits, which were assigned as 1 (reserve > 50 t), 0.75 (50 t > reserve > 10 t), 0.5 (10 t > reserve > 5 t), 0.25 (5 t > reserve > 0 t), and 0 (no deposit found). The activation function was considered to be the logistic function; the learning rate was set to 0.7. The training error curve converged after 277 epochs from an initial square error of 0.072 (Fig. 19). This ensured that the model fits the training data, which is essential in predictive mapping. Finally, combined with the architecture and the saved weights, the BP-ANN model was used to predict the validation units. The results showed that more than 91.3% of total validation units agreed well with the expected value, thus indicating a good classification.

(3) The BP-ANN model prediction. The training and classification were carried out for the remaining prediction units. The output unit generated a value within the range of 0–1; and this could be interpreted as the probability of the presence of uranium at a given location. The probability values of the newly classified feature vectors leaning toward 1 indicated a higher possibility of the presence of minerals in that region. Finally, a potential map was generated by presenting the trained ANN model with an input pattern set (Fig. 20).

(4) Performance test for ANN model. In order to test the performance of the ANN model, the ROC curve was addressed. The results of the ROC analysis, according to different probability threshold values of mineral prospectivity, are shown in Fig. 21. The AUC of the BP-ANN was 0.94, which shows that the ANN model is capable of prospectivity mapping for uranium minerals.

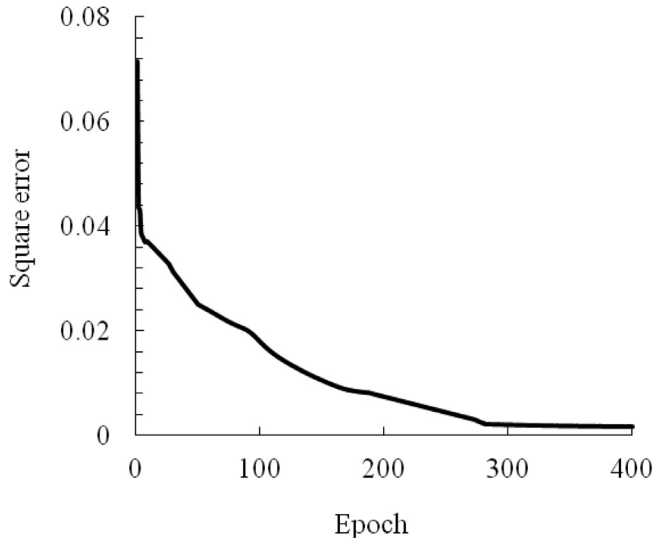

Fig. 19. The evolution of the squared error curve for the supervising data when training the BP-ANN.

6.5. Implications for uranium exploration

Owing to the complexity and fuzzy nature of metallogenic systems and ore-forming processes, the relationship between exploration criteria and certain types of mineral deposits seems to be far too complex to be modeled adequately by using linear approximations in MPM. Compared to other data-driven approaches (e.g. regression approaches), the application of neural networks provides a robust nonlinear alternative to linear approaches for MPM (Porwal et al., 2003b). Accordingly, ANN model can be successfully applied for providing a quantitative measure of the weights among the factors for uranium prospects, because the deposit is usually controlled by a variety of geological features with non-linear relationship. However, there will always be uncertainties in mineral prospectivity model. To reduce these uncertainties, one of the most important procedures involves the selection of appropriate training points. Some criteria have been proposed to define the point locations as follows: (1) deposit vectors and non-deposit vectors should be represented in the same proportion in the set of training vectors; (2) non-deposit vectors should be far from the deposit vectors; and (3) non-deposit vectors should be chaotically distributed (Porwal et al., 2003b; Carranza and Laborte, 2015; Parsa et al., 2018). Exploring significant targeting criteria is also essential to reduce the uncertainties (Carranza et al., 2008). Analysis of the spatial distribution of known mineral deposits associated with evidential features is beneficial to develop calibrated exploration criteria (Kreuzer et al., 2007; Parsa et al., 2018). Table 4 lists the AUC values for each selected evidential layer, which indicate that the exploration criteria were elicited for vectoring toward uranium mineralized zones because of the AUC values being greater than 0.5. The most important criteria are the Nanyuan Formation, followed by fractal dimension anomaly, NE-striking fault and airborne radioactive gamma anomaly. However, owing to the absence of certain exploration evidence data, such as hydrothermal alteration, U/Th variation and F anomaly deemed important in the formation of a volcanogenic uranium deposit (Nash, 2010), the exploration criteria can be further facilitated using supplemental data sets to perfect this prospectivity model. The probability map shows that the high-value areas were consistent with the spatial distribution of ore deposits. Most of the known ore deposits were found to fall in the region of probability having output values greater than 0.20. As a result, most known occurrences were detected, and some unknown areas were clearly delineated by the model, indicating

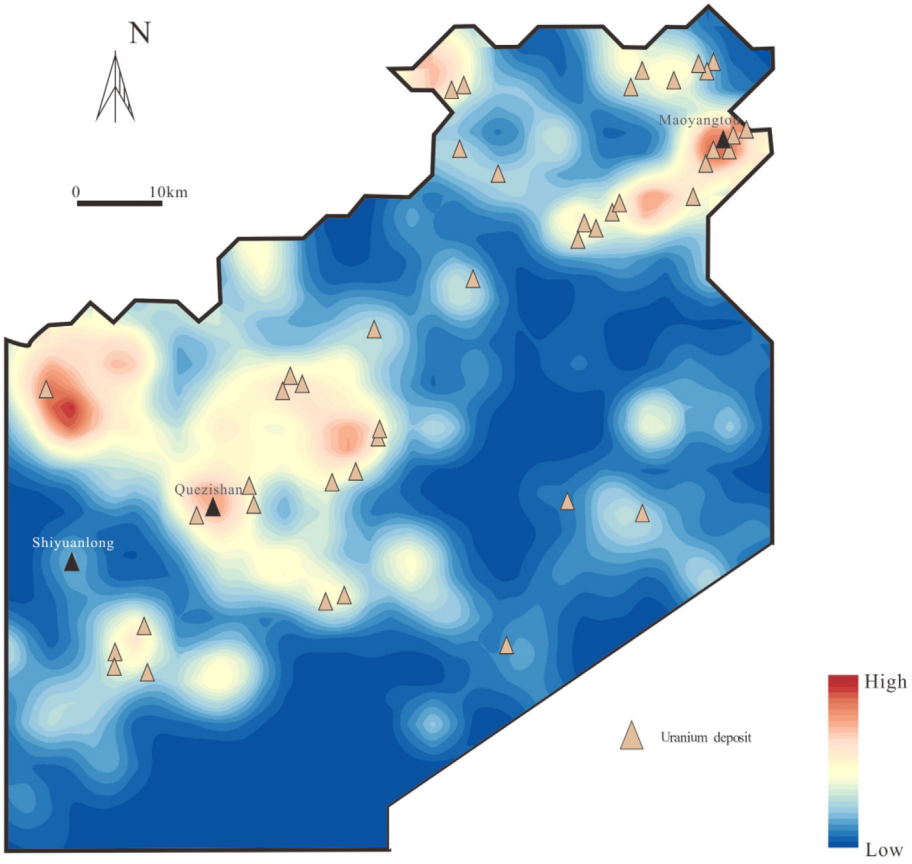

Fig. 20. The probability map obtained by the ANN.

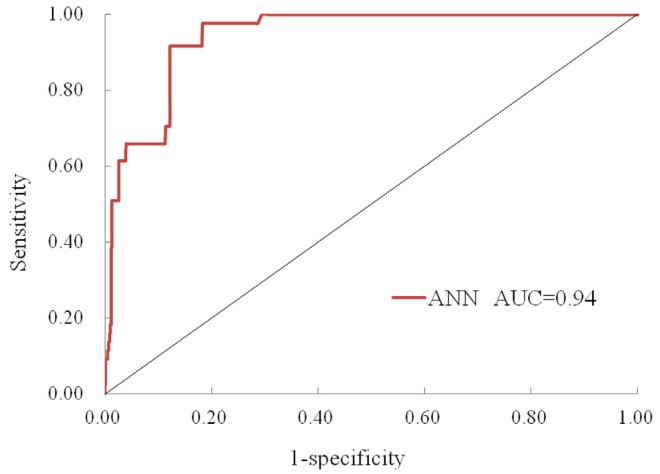

Fig. 21. The ROC curves.

additional potential targets for further exploration. Initial results of this study demonstrate that the ANNs can be effectively used as efficient tools for uranium potential mapping.

7. Conclusions

In this study, various spatial analyses and the ANN model were applied to explore the spatial correlations and map mineral prospectivity for uranium mineralization in Pucheng district, NW Fujian Province, China. The following conclusions were obtained. First, the geological complexity determined by frequency, lengths, the intersection of structures, and fractal dimension by means of box-counting can be used as indexes to characterize the complexity of the spatial distribution of structures. Greater complexity favors uranium deposition, because the more complex structural arrays may have been the ones that captured and focused fluid flow and chemical and physical interactions between the uranium-bearing fluids and their host rocks. Second, the spatial patterns of known mineral occurrences were revealed by *L* function, fractal analysis, and Fry analysis. The results indicate that the ore-bearing fluids might have been transported through the regional-scale NE-, prospect-scale NE- and NW-striking fault pathways. The results are helpful for understanding the mineralization-controlling processes and for weighting the relative importance of geological features on the control of mineral deposit. Finally, the mineral prospectivity maps, generated by the ANN data-driven method, show highly predicted accuracy, indicating the effectiveness of prospectivity mapping of uranium minerals. These predictive maps can provide useful information for further explorations on uranium deposits in Pucheng district.

Acknowledgements

This research was jointly supported by the National Key R&D Program of China (Grant Nos. 2016YFC0600509 & 2017YFC0601504) and the National Natural Science Foundation of China (Grant No. 41302264). The authors especially thank Dr. Oliver Kreuzer for helpful comments on the paper.

References

Agterberg, F.P., Bonham-Carter, G.F., Wright, D.F., 1990. Statistical pattern integration for mineral exploration. In: Daniel, F.Ga.M. (Ed.), GaalComputer Applications in Resource Estimation Prediction and Assessment for Metals and Petroleum. Pergamon Press, Oxford, New York, pp. 1–21.

Asadi, H.H., Sansoleimani, A., Fatehi, M., Carranza, E.J.M., 2016. An AHP–TOPSIS predictive model for district-scale mapping of porphyry Cu–Au potential: a case study from Salafchegan area (Central Iran). Nat. Resour. Res. 25, 1–13.

Baddeley, A., Turner, R., 2005. Spatstat: an R package for analyzing spatial point patterns. J. Stat. Softw. 12, 1–42.

BGMRFJ (Bureau of Geology and Mineral Resources of Fujian Province), 1985. In: Regional geology of Fujian Province. Geological Publishing House, Beijing, pp. 7–564 (in Chinese).

Blenkinsop, T.G., Sanderson, D.J., 1999. Are gold deposits in the crust fractals? A study of gold mines in the Zimbabwean craton. In: McCaffrey, K.J.W., Lonergan, L., Wilkinson, J.J. (Eds.), Fractures, Fluid Flow and Mineralization. Geological Society of London Special Publication, pp. 141–151.

Bonham-Carter, G.F., 1994. Geographic Information Systems for Geoscientists: Modeling with GIS, Computer Methods in the Geosciences 13. Pergamon Press, Oxford, pp. 398.

Bonham-Carter, G.F., Agterberg, F.P., Wright, D.F., 1989. Weights-of-evidence modeling: a new approach to mapping mineral potential. In: Agterberg, F.P., Bonham-Carter, G.F. (Eds.), Statistical Applications in the Earth Sciences. Geological Survey of Canada, pp. 171–183.

Brown, W.M., Gedeon, T.D., Groves, D.I., Barnes, R.G., 2000. Artificial neural networks: a new method for mineral prospectivity mapping. Aust. J. Earth Sci. 47, 757–770.

Cai, Y., Zhang, J., Li, Z., Guo, Q., Song, J., Fan, H., Liu, W., Qi, F., Zhang, M., 2015. Summary of characteristics of uranium resources and metallogenic regularities in China. Acta Geol. Sin. 89, 1051–1069 (in Chinese with English abstract).

Carlson, C.A., 1991. Spatial distribution of ore deposits. Geology 19, 111–114.

Carranza, E.J.M., 2004. Weights of evidence modeling of mineral potential: a case study using small number of prospects, Abra, Philippines. Nat. Resour. Res. 13, 173–187.

Carranza, E.J.M., 2009. Controls on mineral deposit occurrence inferred from analysis of their spatial pattern and spatial association with geological features. Ore Geol. Rev. 35, 383–400.

Carranza, E.J.M., 2011. From predictive mapping of mineral prospectively to quantitative estimation of number of undiscovered prospects. Resour. Geol. 61, 30–51.

Carranza, E.J.M., Laborte, A.G., 2015. Data-driven predictive mapping of gold prospectivity, Baguio district, Philippines: application of Random Forests algorithm. Ore Geol. Rev. 71, 777–787.

Carranza, E.J.M., Sadeghi, M., 2010. Predictive mapping of prospectivity and quantitative estimation of undiscovered VMS deposits in Skellefte district (Sweden). Ore Geol. Rev. 38, 219–241.

Carranza, E.J.M., Woldai, T., Chikambwe, E.M., 2005. Application of data-driven evidential belief functions to prospectivity mapping for aquamarine-bearing pegmatites, Lundazi district, Zambia. Nat. Resour. Res. 14, 47–63.

Carranza, E.J.M., Hale, M., Faassen, C., 2008. Selection of coherent deposit-type locations and their application in data-driven mineral prospectivity mapping. Ore Geol. Rev. 33, 536–558.

Carranza, E.J.M., Owusu, E., Hale, M., 2009. Mapping of prospectivity and estimation of number of undiscovered prospects for Lode-gold, southwestern Ashanti Belt, Ghana. Miner. Deposita 44, 915–938.

Chen, D., 1997. Ore-controlling factors and genesis of Maoyangtou volcanic U (Ag, Mo) deposit. Miner. Deposits 16, 44–55 (in Chinese with English abstract).

Chen, D., Zhang, B., Chen, P., 1995. Characteristics of major ore minerals in 570 deposit. Acta Mineral. Sin. 15, 271–275 (in Chinese with English abstract).

Chen, D., Sun, D., Zhang, B., 1997. Isotope geochemistry of Maoyangtou uranium (silver & molybdenum) deposit. Geochemistry 26, 29–37 (in Chinese with English abstract).

Cheng, Q., Agterberg, F.P., 1999. Fuzzy weights of evidence method and its application in mineral potential mapping. Nat. Resour. Res. 8, 27–35.

Cox, S.F., Knackstedt, M.A., Braun, J., 2001. Principles of structural control on permeability and fluid flow in hydrothermal systems. Structural Controls on Ore Genesis. Rev. Econ. Geol. 14, 1–14.

Diggle, P.J., 1983. Statistical Analysis of Spatial Point Patterns. Academic Press, London, pp. 148.

Du, X., Zhou, K., Cui, Y., Yao, C., Wang, N., Zhang, W., 2016. Application of fuzzy analytical herarchy process (AHP) and prediction-area (P-A) plot for mineral prospectivity mapping: a case study from the Dananhu metallogenic belt, Xinjiang, NW China. Arab. J. Geosci. 9, 298.

Fallon, M., Porwal, A., Guj, P., 2010. Prospectivity analysis of the plutonic Marymia greenstone belt, Western Australia. Ore Geol. Rev. 38, 208–218.

Finch, W.I., Feng, S., Zuyi, C., Mccammon, R.B., 1993. Descriptive models of major uranium deposits in China. Nonrenew. Resour. 2, 39–48.

Ford, A., Blenkinsop, T.G., 2008. Evaluating geological complexity and complexity gradients as controls on copper mineralization, Mt Isa Inlier. Aust. J. Earth Sci. 55, 13–23.

Ford, A., Miller, J.M., Mol, A.G., 2016. A comparative analysis of weights of evidence, evidential belief functions, and fuzzy logic for mineral potential mapping using incomplete data at the scale of investigation. Nat. Resour. Res. 25, 19–33.

Fry, N., 1979. Random point distributions and strain measurement in rocks. Tectonophysics 60, 89–105.

Fu, J., Zhao, N., Pei, C., Li, X., 2015. Characteristics of indicator elements combination and genesis of four types of uranium mineralization in China. Geophys. Geochem. Explor. 39, 217–221 (in Chinese with English abstract).

Harris, J.R., Grunsky, E., Behnia, P., Corrigan, D., 2015. Data-and knowledge-driven mineral prospectivity maps for Canada's North. Ore Geol. Rev. 71, 788–803.

Hengl, T., 2006. Finding the right pixel size. Comput. Geosci. 32, 1283–1298.

Hodkiewiczi, P.F., Weinberg, R.F., Gardoll, S.J., Groves, D.I., 2005. Complexity gradients in the Yilgarn Craton: fundamental controls on crustal-scale fluid flow and the formation of world-class orogenic-gold deposits. Aust. J. Earth Sci. 52, 831–841.

Hou, B., Keeling, J., Li, Z., 2017. Paleovalley-related uranium deposits in Australia and China: a review of geological and exploration models and methods. Ore Geol. Rev. 88, 201–234.

Huang, Y., 2010. Mineralization of Xiandian-Pucheng thrust belt in Wuyishan, Fujian. Fujian Geol. 29, 217–223 (in Chinese with English abstract).

Huang, Z., Williamson, A., 1996. Artificial neural network modeling as an aid to source

rock characterization. Mar. Pet. Geol. 13, 277–290.
Kreuzer, O.P., Blenkinsop, T.G., Morrison, R.J., Peters, S.G., 2007. Ore controls in the Charters Towers goldfield, NE Australia: constraints from geological, geophysical and numerical analyses. Ore Geol. Rev. 32, 37–80.
Kreuzer, O.P., Markwitz, V., Porwal, A.K., McCuaig, T.C., 2010. A continent-wide study of Australia's uranium potential. Ore Geol. Rev. 38, 334–366.
Leite, E.P., de Souza, Filho, Roberto, Carlos, 2009. Artificial neural networks applied to mineral potential mapping for copper-gold mineralizations in the Carajás Mineral Province, Brazil. Geophys. Prospect. 57, 1049–1065.
Leroy, J.L., George-Aniel, B., 1992. Volcanism and uranium mineralizations: the concept of source rock and concentration mechanism. J. Volcanol. Geoth. Res. 50, 247–272.
Li, W., Liu, R., Fang, X., Zhang, W., 2012. Relationship between the genesis of uranium deposits and the fault structures in Chong'an district. Uranium Geol. 28, 215–221 (in Chinese with English abstract).
Lisitsin, V.A., Porwal, A., Mccuaig, T.C., 2014. Probabilistic Fuzzy Logic Modeling: quantifying uncertainty of mineral prospectivity models using Monte Carlo simulations. Math. Geosci. 46, 747–769.
Liu, R., Zhou, H., Zhang, L., Zhong, Z., Zeng, W., Xia, H., Jin, S., Lu, X., Li, C., 2010. Zircon U-Pb ages and Hf isotope compositions of the Mayuan migmatite complex, NW Fujian Province, Southeast China: constraints on the timing and nature of a regional tectonothermal event associated with the Caledonian orogeny. Lithos 119, 163–180.
Lou, Z., 2013. Geological characteristics and metallogenic prospects of the Quezishan uranium deposit in Wuyishan, Fujian Province. J. East China Univ. Technol. 36, 265–273 (in Chinese with English abstract).
Lu, W., Wang, Y., 1990. Isotope geochemistry of 570 uranium deposit, Fujian. J. Chengdu Univ. Technol. 17, 85–93 (in Chinese with English abstract).
Lu, W., Yang, S., Zhang, P., Wang, Y., 1997. Isotope geological characteristics of uranium deposits in Shiyuanlong area. J. Mineral. Petrol. 17, 69–76 (in Chinese with English abstract).
Maithani, P.B., Srinivasan, S., 2011. Felsic volcanic rocks, a potential source of uranium-an Indian overview. Energy Procedia 7, 163–168.
Mandelbrot, B.B., 1983. The Fractal Geometry of Nature. Freeman, New York, pp. 495.
McCuaig, T.C., Beresford, S., Hronsky, J., 2010. Translating the mineral systems approach into an effective exploration targeting system. Ore Geol. Rev. 38, 128–138.
Müller, B., Reinhardt, J., Strickland, M.T., 1995. Neural Networks: An Introduction, second ed. Springer-Verlag, New York.
Nash, J. Thomas, 2010. Volcanogenic uranium deposits—Geology, geochemical processes, and criteria for resource assessment: U.S. Geological Survey Open-File Report 2010-1001, 99 p.
Nie, G., Yin, L., Wang, X., Liu, L., 1994. Formation conditions and tectonic environment of mesozoic uranium and polymetallic deposits in Pucheng, Fujian Province. J. East China Univ. Technol. 2, 106–116 (in Chinese with English abstract).
Oh, H., Lee, S., 2010. Application of artificial neural network for gold-silver deposits potential mapping: a case study of Korea. Nat. Resour. Res. 19, 103–124.
Parsa, M., Maghsoudi, A., 2018. Controls on Mississippi valley-type Zn-Pb mineralization in Behabad district, central Iran: constraints from spatial and numerical analyses. J. Afr. Earth Sci. 140, 189–198.
Parsa, M., Maghsoudi, A., Yousefi, M., 2018. Spatial analyses of exploration evidence data to model skarn-type copper prospectivity in the Varzaghan district, NW Iran. Ore Geol. Rev. 92, 97–112.
Pérez-López, R., Paredes, C., Muñoz-Martín, 2005. Relationship between the fractal dimension anisotropy of the spatial faults distribution and the paleostress fields on a Variscan granitic massif (Central Spain): the F-parameter. J. Struct. Geol. 27, 663–677.
Porwal, A., Carranza, E.J.M., Hale, M., 2003a. Knowledge-driven and data-driven fuzzy models for predictive mineral potential mapping. Nat. Resour. Res. 12, 1–25.
Porwal, A., Carranza, E.J.M., Hale, M., 2003b. Artificial neural networks for mineral potential mapping. Nat. Resour. Res. 12, 155–171.
Porwal, A., Das, R.D., Chaudhary, B., Gonzalez-Alvarez, I., Kreuzer, O., 2015. Fuzzy inference systems for prospectivity modeling of mineral systems and a case-study for prospectivity mapping of surficial Uranium in Yeelirrie Area, Western Australia. Ore Geol. Rev. 71, 839–852.
Porwal, A.K., Kreuzer, O.P., 2010. Introduction to the special issue: mineral prospectivity analysis and quantitative resource estimation. Ore Geol. Rev. 38, 121–127.
Raines, G.L., 2008. Are fractal dimensions of the spatial distribution of mineral deposits meaningful? Nature Resour. Res. 17, 87–97.
Ripley, B., 1977. Modelling spatial patterns (with discussion). J. Roy. Stat. Soc. B 39, 172–212.
Shen, H., Wang, Z., Gao, C., Qin, Juan., Yao, F., X, W., 2008. BP neural network hidden layer unit number determination. Journal of Tianjin University of Technology 24, 13–15 (in Chinese with English abstract).
Thompson, S., Fueten, F., Bockus, D., 2001. Mineral identification using artificial neural networks and the rotating polarizer stage. Comput. Geosci. 27, 1081–1089.
Turcotte, D.L., 1992. Fractals and Chaos in Geology and Geophysics. Cambridge University Press, Cambridge, pp. 412.
Vearncombe, J., Vearncombe, S., 1999. The spatial distribution of mineralization: applications of Fry analysis. Econ. Geol. 94, 475–486.
Velde, B., Dubois, J., Touchard, G., Badri, A., 1990. Fractal analysis of fractures in rocks: the Cantor's Dust. Tectonophysics 179, 345–352.
Walsh, J.J., Watterson, J., 1993. Fractal analysis of fracture patterns using the standard box-counting technique: valid and invalid methodologies. J. Struct. Geol. 15, 1509–1512.
Wang, Y., Li, W., Zheng, S., Yang, Y., Huang, Z., 1990. Controlling factors and ore forming conditions of 570 ore deposit. Uranium Geol. 6, 1–10 (in Chinese with English abstract).
Wang, C., Rao, J., Chen, J., Ouyang, Y., Qi, S., Li, Q., 2017. Prospectivity mapping for "Zhuxi-type" copper-tungsten polymetallic deposits in the Jingdezhen region of Jiangxi province, south China. Ore Geol. Rev. 89, 1–14.
Wang, Z., Zuo, R., Zhang, Z., 2015. Spatial analysis of Fe deposits in Fujian province, China: implications for mineral exploration. J. Earth Sci. 26, 813–820.
Wei, D., Jie, Y., Huang, T., 1997. Regional geological structural characteristics of Fujian province. Regional Geol. China 2, 51–59 in Chinese with English abstract.
Wyborn, L.A.I., Heinrich, C.A., Jaques, A.L., 1994. Australian Proterozoic mineral systems: essential ingredients and mappable criteria. In: Australian Institute of Mining and Metallurgy Annual Conference, Melbourne, Proceedings, pp. 109–115.
Xiao, B., Wang, Y., 1998. Prospects for volcanic-type uranium mineralization in Pucheng area. J. East China Geol. Inst. 21, 15–20 (in Chinese with English abstract).
Yousefi, M., Carranza, E.J.M., 2017. Union score and fuzzy logic mineral prospectivity mapping using discretized and continuous spatial evidence values. J. Afr. Earth Sci. 128, 47–60.
Yousefi, M., Nykänen, V., 2017. Introduction to the special issue: GIS-based mineral potential targeting. J. Afr. Earth Sci. 128, 1–4.
Zhang, W., 1986. Geochemical characteristics of metamorphic volcanic rocks in northwestern Fujian. Fujian Geol. 5, 36–50 (in Chinese with English abstract).
Zhang, Q., Lin, Y., Xu, S., Chen, J., Du, J., Ge, R., 2008. A new view on division of terranes and their tectonic evolution in Fujian province. Resour. Survey Environ. 29, 168–176 (in Chinese with English Abstract).
Zhang, Z., Zuo, R., Xiong, Y., 2016. A comparative study of fuzzy weights of evidence and random forests for mapping mineral prospectivity for skarn-type Fe deposits in the southwestern Fujian metallogenic belt, China. Sci. China Earth Sci. 59, 556–572.
Zhao, J., Chen, S., Zuo, R., Carranza, E.J.M., 2011. Mapping complexity of spatial distribution of faults using fractal and multifractal models: vectoring towards exploration targets. Comput. Geosci. 37, 1958–1966.
Zhao, J., Zuo, R., Chen, S., Kreuzer, O.P., 2015. Application of the tectono-geochemistry method to mineral prospectivity mapping: a case study of the Gaosong tin-polymetallic deposit, Gejiu district, SW China. Ore Geol. Rev. 71, 719–734.
Zhao, J., Chen, S., Zuo, R., 2016. Identifying geochemical anomalies associated with Au–Cu mineralization using multifractal and artificial neural network models in the Ningqiang district, Shaanxi, China. J. Geochem. Explor. 164, 54–64.
Zhao, K., Jiang, S., Chen, W., Chen, P., Ling, H., 2013. Zircon U-Pb chronology and elemental and Sr–Nd–Hf isotope geochemistry of two Triassic A-type granites in South China: implication for petrogenesis and Indosinian transtensional tectonism. Lithos 160–161, 292–306.
Zhou, M., 2010. Geological characteristics and prospecting prospects of the Maoyangtou uranium deposit in Pucheng, Fujian. Fujian Geol. 29, 8–16 (in Chinese with English abstract).
Zhou, M., 2012. Ore-forming information extraction and mineralization quantitative prediction for volcanic uranium deposits in Pucheng-Chongan district, Fujian Provinces. Master dissertation unpublished, China University of Geosciences, Wuhan, pp: 1-45 (in Chinese).
Zuo, R., 2016. A nonlinear controlling function of geological features on magmatic-hydrothermal mineralization. Sci. Rep. 6, 27127.
Zuo, R., Cheng, Q., Agterberg, F.P., 2009a. Application of a hybrid method combining multilevel fuzzy comprehensive evaluation with asymmetric fuzzy relation analysis to mapping prospectivity. Ore Geol. Rev. 2009, 101–108.
Zuo, R., Agterberg, F.P., Cheng, Q., Yao, L., 2009b. Fractal characterization of the spatial distribution of geological point processes. Int. J. Appl. Earth Obs. Geoinf. 11, 394–402.
Zuo, R., Carranza, E.M.J., 2011. Support vector machine: a tool for mapping mineral prospectivity. Comput. Geosci. 37, 1967–1975.
Zuo, R., Carranza, E.J.M., 2017. A fractal measure of spatial association between landslides and conditioning Factors. J. Earth Sci. 28, 588–594.